In Vivo Positronium Lifetime Measurements with a Long Axial Field-of-View PET/CT

Lorenzo Mercolli[1,2*], William M. Steinberger[3], Hasan Sari[1,2,4], Ali Afshar-Oromieh[1], Federico Caobelli[1], Maurizio Conti[3], Ângelo R. Felgosa Cardoso[1], Clemens Mingels[1], Paweł Moskal[5,6], Thomas Pyka[1], Narendra Rathod[1,2], Robin Schepers[1], Robert Seifert[1], Kuangyu Shi[1,2], Ewa Ł. Stępień[5,6], Marco Viscione[1], Axel O. Rominger[1]

[1]Department of Nuclear Medicine, Inselspital, Bern University Hostpital, University of Bern, Bern, Switzerland.
[2]ARTORG Center for Biomedical Engineering Research, University of Bern, Bern, Switzerland.
[3]Siemens Medical Solutions USA, Inc., Knoxville TN, USA.
[4]Siemens Healthineers International AG, Zürich, Switzerland.
[5]Faculty of Physics, Astronomy and Applied Computer Science, Jagiellonian University, Krakow, Poland.
[6]Centre for Theranostics, Jagiellonian University, Krakow, Poland.

*Corresponding author(s). E-mail(s): lorenzo.mercolli@insel.ch;
Contributing authors: william.steinberger@siemens-healthineers.com; hasan.sari@unibe.ch; ali.afshar@insel.ch; federico.caobelli@insel.ch; maurizio.conti@siemens-healthineers.com; angelo.cardoso@insel.ch; clemens.mingels@insel.ch; p.moskal@uj.edu.pl; thomas.pyka@insel.ch; narendra.rathod@unibe.ch; robin.schepers@extern.insel.ch; robert.seifert@insel.ch; kuangyu.shi@insel.ch; e.stepien@uj.edu.pl; marco.viscione@insel.ch; axel.rominger@insel.ch;

Abstract

Purpose: The lifetime of orthopositronium (oPs), a spin triplet of an electron and positron, depends on the molecular structure of the surrounding tissue. Therefore, measuring oPs lifetime could in principle provide diagnostic information about the tissue microenvironment that goes beyond standard positron

emission tomography (PET) imaging. This study demonstrates that in vivo oPs lifetime measurement is feasible with a commercial long axial field-of-view (LAFOV) PET/CT scanner.

Methods: Three subjects received a dose of 148.8 MBq [^{68}Ga]-Ga-DOTA-TOC, 159.7 MBq [^{68}Ga]Ga-PSMA-617 and 420.7 MBq [^{82}Rb]Cl. In addition to the standard protocol, the three subjects were scanned for 20, 40 and 10 minutes with a single-crystal interaction acquisition mode on a Biograph Vision Quadra (Siemens Healthineers) PET/CT. Three-photon events, that include two annihilation photons and a prompt photon from the decay of the radionuclide, are then selected from the list mode data based on energy, time and spatial selection criteria using a prototype software. The spatial location of the annihilation events is reconstructed using the annihilation photons' time-of-flight. Through a Bayesian fit to the measured time difference between the annihilation and the prompt photons, we are able to determine the oPs lifetime for selected organs. The Bayesian fitting methodology is extended to a hierarchical model in order to investigate possible common oPs lifetime distributions of the heart chambers in the [^{82}Rb]Cl scan.

Results: From the segmentation of the subjects' histoimages of three-photon events, we present the highest density intervals (HDI) of the oPs lifetime's marginalized posterior distribution for selected organs. Interestingly, the mean values of the right heart chambers were higher than in the left heart chambers of the subject that received [^{82}Rb]Cl: the 68% HDI of the atria are [1.15 ns, 1.72 ns] (left) and [1.46 ns, 1.99 ns] (right) with mean values 1.50 ns and 1.76 ns, respectively. For the ventricles we obtained [1.22 ns, 1.60 ns] (left) and [1.69 ns, 2.18 ns] (right) with mean values 1.44 ns and 1.96 ns. This might signal the different oxygenation levels of venous and arterial blood. Fitting a hierarchical model, we found that the oPs lifetime for volumes-of-interest with arterial blood can be sampled form a posterior distribution with a 68% HDI of [1.4 ns, 1.84 ns] (mean 1.62 ns) and while those containing venous blood have a HDI of [1.78 ns, 2.21 ns] (mean 2.0 ns). Through arterial and venous blood sampling, we were unable to confirm such a difference in the oPs lifetime.

Conclusion: In vivo oPs lifetime measurements on a commercial LAFOV PET/CT system are feasible at the organ level with an unprecedented level of statistical power. Nevertheless, count statistics of three-photon events (especially for ^{68}Ga-based measurements) and the interpretation of oPs lifetimes in human tissue remain major challenges that need to be addressed in future studies.

Keywords: Positronium, Long axial field-of-view PET/CT, [82Rb]Cl, [68Ga]-PSMA-617, [68Ga]-DOTA-TOC

1 Introduction

Positronium (Ps), the bound state of an electron and a positron, has been an object of investigation since its theoretical conception by Stjepan Mohorovičić in 1934 [1] and its discovery by Martin Deutsch in 1951 [2]. The absence of leading order hadronic interactions in Ps allowed for precision tests of bound state quantum electrodynamics and related models (see e.g. Ref. [3, 4] and references therein).

In Ps, the electron's and positron's spins add up to either 0 or 1, yielding a singlet and triplet state

$$\frac{1}{\sqrt{2}}\left(|\uparrow\downarrow\rangle - |\downarrow\uparrow\rangle\right) \qquad \text{and} \qquad |\uparrow\uparrow\rangle \ , \ \frac{1}{\sqrt{2}}\left(|\uparrow\downarrow\rangle + |\downarrow\uparrow\rangle\right) \ , \ |\downarrow\downarrow\rangle \ . \tag{1}$$

The singlet state is called parapositronium (pPs) and the triplet state orthopositronium (oPs). The distinctive feature of Ps compared to a hydrogen atom is the possibility to annihilate. pPs and oPs are odd and even eigenstates of charge conjugation and parity transformations. The corresponding selection rule therefore implies that the dominant annihilation mode for pPs is in two photons, while oPs will annihilate into three photons. Even using the most naïve Ps decay model from J. Pirenne and J. A. Wheeler (see e.g. Ref. [3]), the decay constant of oPs in vacuum is almost three orders of magnitude times smaller than the decay constant of pPs

$$\frac{\Gamma(oPs \to \gamma\gamma\gamma)}{\Gamma(pPs \to \gamma\gamma)} \ = \ \frac{\frac{2\alpha^6 m\,(\pi^2-9)}{9\pi}}{\frac{\alpha^5 m}{2}} \ \approx \ 8.99 \cdot 10^{-4} \ , \tag{2}$$

where m is the electron/positron mass and α the finestructure constant. Intuitively, the ratio scales as $\propto \alpha \approx 1/137$ and in addition there is the larger three-body phase space of the final state.

Being relative long-lived, oPs has enough time undergo interactions with surrounding material. The so-called *pick-off* process describes the oPs annihilation into two γ from an interaction with an environmental electron (see e.g. Refs. [5–7]). Such a pick-off shortens the oPs lifetime significantly and introduces a dependence on the physical and chemical environment. Apart from the pick-off process, spin exchange with unpaird electrons can also lead to a conversion from oPs to pPs and thus a two γ annihilation. The oPs annihilation into two photons therefore becomes a surrogate quantity for the molecular structure of the surrounding material. It should be noted that also the probability for Ps to form depends on environmental conditions.

The measurement of oPs lifetime is often termed *positron lifetime spectroscopy* (PALS). It can provide detailed information about defects in solids, lattice imperfections in semiconductors, free volumes and structures in polymers (see e.g. Refs. [5, 8–13]). The high sensitivity to a material's structure and relatively simple experimental setups made PALS a widely adopted technique in material science.

For more than a decade, the medical domain has shown significant interest in PALS (see e.g. Refs. [6, 7, 14–22]). Driven by the possibility to measure oxygenation levels in human tissue [23–28], several in vitro studies were performed by the authors of Refs. [15, 19, 29]. Recently, the first in vivo measurement of oPs lifetimes was reported in Ref. [30]. The oPs lifetime has the potential to add diagnostic information which is currently unavailable or requires additional interventions, such as e.g. biopsy or additional use of hypoxia tracers.

A key factor in exploring the clinical potential of oPs lifetime measurements is the ability to use standard positron emission tomography (PET) scanners [31]. Standard PET/CT scanners are devised and optimized to detect two coinciding 511 keV photons

from the positron annihilation. However, the oPs lifetime is determined through the measurement of the time difference between the detection of two annihilation photons and a prompt photon from the mother nuclide's decay. This means that we need to identify three-photon events (3γE) rather that just two-photon coincidences (and that such measurements can be done only with non-pure positron emitters [32, 33]). Therefore, we need to be able to detect, store and process single photon interactions in the PET detector in order to measure the oPs lifetime, as introduced e.g. in Ref. [34] for the J-PET detector with the trigger-less data acquisition.

Another major challenge in PALS measurement is the collection of enough 3γE. Typical PALS measurement use long-lived radionuclides with a high prompt gamma branching fraction, like e.g. ^{22}Na, and data collection can last for many hours. However, radionuclides used in clinical routine have only a limited prompt photon branching fraction (see Tab. 2), if any at all, and scan time is limited by either a short half-life, as in the case of ^{82}Rb, or by the time a patient is able to stay in the scanner. This is why only long axial field-of-view (LAFOV) PET/CT systems stand a chance to collect the necessary count statistics for a Ps lifetime measurement. This kind of systems has entered clinical routine operation a couple of years ago (see e.g. Refs. [35, 36]) and has shown to have a significant increase in sensitivity over standard axial field-of-view scanners [37, 38]. Note that also the image reconstruction process for 3γE has triggered substantial research, as shown e.g. in Refs. [39–44], in order to address the problem of limited count statistics.

In order to capitalize on the potential of oPs lifetime measurements in patients, the capability of clinical LAFOV PET/CT systems to perform this kind of measurements needs to be shown. Recently, we showed in Refs. [45, 46] that it is possible to determine the oPs lifetime in reference materials with a Siemens Biograph Vision Quadra (Siemens Healthineers, Hoffman Estates, IL, USA) (henceforth simply referred to as Quadra) with the clinically used radionuclides ^{68}Ga, ^{124}I and ^{82}Rb. Quadra has a prototype feature that allows for a trigger-less acquisition mode, the so called *singles mode*, where single-crystal interactions within a given mini-block detector are saved without coincidence sorting into to a list mode file. The 3γE selection can then be done off-line.

In the present publication we present the first in vivo Ps lifetime measurements with a commercial LAFOV PET/CT system. We acquired data in singles mode from three subjects that received a standard dose of [^{68}Ga]Ga-PSMA-617, [^{68}Ga]Ga-DOTA-TOC and [^{82}Rb]Cl (seel Tab. 1). Using the event selection algorithm presented in Ref. [46], we determine the time difference spectra for different organs. Through a Bayesian fitting procedure we are able to measure the oPs lifetime for different organs. Within the Bayesian framework, we develop a hierarchical model to combine 3γE from different volume-of-interest (VOI). This shows that organ-level PALS measurements are possible with an unprecedented level of count statistics.

2 Materials and methods

2.1 Study subjects and scan protocols

This study includes two patients and a healthy volunteer. The personal details are given in Tab. 1. The subjects were administered with different compounds with ^{68}Ga and ^{82}Rb. Both radionuclides emit prompt photons, as can be seen in Tab. 2. Note that the prompt photon intensity for these radionuclides is rather low. Other radionuclides in clinical use, like ^{124}I or ^{89}Zr, have a much higher branching fraction for prompt photons.

Table 1: Details of the three subjects and administered activities.

Subject	Weight [kg]	Radiopharm.	Activity [MBq]
S1	71	[^{68}Ga]Ga-DOTA-TOC	148.8
S2	78	[^{68}Ga]Ga-PSMA-617	159.7
S3	80	[^{82}Rb]Cl	420.7

Table 2: Decay properties of ^{68}Ga, ^{82}Rb and ^{124}I together with the main prompt photon energy and branching ratio according to Refs. [47–49].

Nuclide	Decay mode	Decay const. [s^{-1}]	E_γ [keV]	Branching ratio [%]
^{68}Ga	ec β^+ 100 %	$(1.706 \pm 0.002) \cdot 10^{-4}$	1077.37 ± 0.04	3.22 ± 0.03
^{82}Rb	ec β^+ 100 %	$(9.1868 \pm 0.0015) \cdot 10^{-3}$	776.511 ± 0.10	15.1 ± 0.3
^{124}I	ec β^+ 100 %	$(1.92111 \pm 0.00014) \cdot 10^{-6}$	602.73 ± 0.08	62.9 ± 0.7

A patient (referred to as S1 in the following) with multifocal meningioma was administered 148.8 MBq of [^{68}Ga]Ga-DOTA-TOC. A 10 min acquisition in coincidence mode, i.e. a standard clinical scan with two-photon coincidence sorting, was performed 32 min p.i. (see Tab. 3). The dose-length-product (DLP) of the CT scan was 558 mGy·cm. At 44 min p.i. the singles mode scan was started and lasted 20 min. Fig. 1 shows the coronal and sagittal maximum intensity projections (MIP) of coincidence PET image.

The second patient S2 was referred to our clinic with prostatic adenokarzinoma and a suspected local recurrence. He had undergone a prostatectomy about three years prior to the this study. The patient received 159.7 MBq [^{68}Ga]Ga-PSMA-617 and was scanned for 13 min in coincidence mode about two hours p.i. As summarized in Tab. 3, the singles mode scan lasted for 40 min and started prior to the clinical PET/CT scan. The DLP was 244 mGy · cm. The early coincidence PET image is shown in Fig. 1.

Finally, the subject S3 obtained 420.7 MBq [^{82}Rb]Cl. The [^{82}Rb]Cl was produced with CardioGen-82 radionuclide generator and infusion system (Bracco Imaging S.p.A, Milan, Italy). Due to the short half-life of ^{82}Rb, only the singles mode acquisition and a low-dose CT with a DLP of 268 mGy · cm scan were performed for S3. The infusion

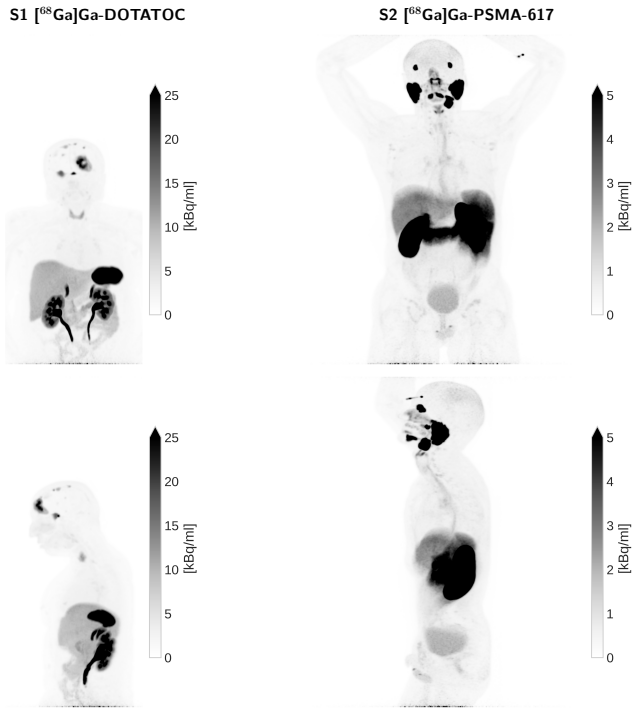

Fig. 1: Coronal (top) and sagittal (bottom) MIP of the coincidence PET images for S1 (left) and S2 (right).

of the [^{82}Rb]Cl started simultaneously with the singles mode acquisition and lasted for 19 s.

Table 3: Start time and duration of the singles and coincidence PET scans.

Subject	Coincidence [min]	Start coincidence [min]	Singles [min]	Start singles [min]
S1	10	32 p.i.	20	44 p.i.
S2	13	123 p.i.	40	18 p.i.
S3	-	-	10	0 p.i.

We evaluate several organs for oPs lifetime measurement across all three subjects, including the kidneys, liver, lungs, pancreas, and spleen. In addition, specific organs are segmented for each subject: S1 had the meningioma segmented; S2 included the parotid gland. The suspected local recurrence in S2 is too small to provide a sufficient number of 3γE for analysis. For S3, the additional VOI are the aorta, right axillary vein, brain, thyroid, and the four heart chambers. Most segmentations are performed on CT images using the AI-based TotalSegmentator tool [50, 51]. An experienced nuclear medicine clinician reviewed and amended the automatic segmentations wherever needed. The meningioma in S1 is segmented using the coincidence PET image

and the axillary vein in S3 is directly segmented using the histoimage of 3γE (image with number of detected 3γE as voxel value).

We also investigated blood samples from S3. We scanned a syringe with 20 ml venous blood mixed with about 45.3 MBq and 3 ml [^{82}Rb]Cl for 10 minutes, starting 5 minutes after the withdrawal of the venous blood sample. In addition, two samples of 1.5 ml venous blood were taken in a syringe that is used for blood gas analyses, i.e. which contains a small heparin plate. About 0.04 ml [^{124}I]NaI with 2.94 MBq (venous blood sample) and 4.32 MBq (arterial blood sample) were added and data was acquired for 15 min. About 25 min passed between the blood sampling and the singles mode scan. After the singles mode scan, a 15 min coincidence mode scan was performed. After the experiment, the ^{124}I activities in the syringes were measured with a well-type dose calibrator and decay-corrected to the start time of the singles mode scan.

2.2 Time difference measurements

The details of the 3γE selection and time difference measurements with Quadra are discussed Refs. [45, 46]. In singles mode, Quadra registers all detector hits without any triggering or event sorting and writes the photon energy, time stamp and crystal ID into a list-mode file. A prototype software groups all possible combinations of three detector events within a time window of 20 ns into a 3γE. In a second step, all 3γE that do not fall within a given energy window are discarded. Two energy windows need to be selected: one for the two annihilation photons and one for the prompt photon. For both ^{68}Ga and ^{82}Rb, we set the energy window for the annihilation photons from 435 to 585 keV and the prompt photon window from 720 to 726 keV. As explained in Ref. [46], the last energy bin collects all detector hits from higher energies up to approximately 950 keV, i.e. despite ^{68}Ga and ^{82}Rb emitting photons with energies higher than 726 keV (see Tab. 2) they are detected by Quadra. For the ^{124}I sample, the energy windows is chosen from 468 to 545 keV and from 568 to 639 keV. Quadra can fully resolve the prompt photon's photopeak for ^{124}I. Next, the two annihilation photons must be detected within a coincidence time window of 4.2 ns for the 3γE not to be discarded. Finally, a threshold on the minimum distance between the detection location of the prompt and annihilation photons is enforced. Due to the spatial correlation of the detector hits originating from the ^{176}Lu background in Quadra's LSO crystals, this spatial threshold effectively removes false 3γE from crystal radiation (see Ref. [46] for details).

Once the 3γE are sorted, the spatial location of the 3γE is reconstructed with the time-of-flight information of the two annihilation photons. From the 3γE location and the flight path of the prompt photon, it is then straight forward to determine the time difference between the prompt photon emission and positron annihilation. The histograms of the measured time differences for all 3γE in a VOI are the time difference distributions (TDD). We do not account for the attenuation of photons in the subject's bodies. Rescaling the number of detected photons by an attenuation map would likely rescale a TDD but not significantly change its shape.

2.3 Data analysis

After the positron is emitted from the decaying nucleus, it undergoes many different processes and states before annihilating with an electron. Therefore, measured TDD contains many different components that we have to disentangle. Depending on the time scale, it is possible to neglect some of these components.

The radionuclides in Tab. 2 emit positrons with an expectation value for the kinetic energies of 836.0 ± 0.6, 1536.0 ± 1.5 and 687.0 ± 9 keV for ^{68}Ga, ^{82}Rb and ^{124}I, respectively (as computed through Ref. [52]). At first, the positrons will loose their energies mostly through interactions with the surrounding atoms (Bremsstrahlung, ionizations and inelastic collisions). At low energies, the annihilation cross section is proportional to $\propto (1+\mathcal{O}(\beta))/\beta$, making a direct in-flight annihilation unlikely. It takes a 1.5 MeV positron about $\mathcal{O}(20\,\mathrm{ps})$ to slow down to $O(10\,\mathrm{eV})$ in water. This time scale is rather short and is typically neglected in PALS measurements. Its effect in TDD is typically absorbed in the modelling of the measurement device. The Ps formation cross section peaks around 10 eV, as shown e.g. in Ref. [53]. If no Ps formation occurred, the positron will thermalize through elastic interactions and eventually annihilate with an electron. The thermalization process can take $\mathcal{O}(400\,\mathrm{ps})$ and cannot be neglected. One component of the TDD is therefore the direct annihilation without Ps formation.

Once a Ps state is formed, there are multiple possibilities for an annihilation into two photons, as illustrated e.g. in Fig. 1 of Ref. [23]. On average, pPs annihilates into two photons within $\approx 2/(\alpha^5 m) \approx 125\,\mathrm{ps}$ without being particularly affected by the environment. oPs can either turn into pPs through spin exchange or annihilate into two photons through a pick-off process. Since all annihilations in two photons are detected, both $\Gamma(\mathrm{pPs} \to \gamma\gamma)$ and $\Gamma(\mathrm{oPs} + e^- \to \gamma\gamma)$ are contributing to the measured TDD. The annihilation of oPs into three photons is not contained in the TDD since we do not sort four-photon events. In order to determine the oPs lifetime from the TDD, we therefore need to consider three components: direct annihilation together pPs and oPs decay.

Note that the time difference measurement outlined in Sec. 2.2 assumes that the prompt photon emission has a negligible delay compared to the positron emission. This assumption is valid for the radionuclides in Tab. 2, since the 2^+ states of ^{68}Zn, ^{82}Kr and ^{124}Te have half-lives of 1.61 ± 0.2 ps [47], 4.45 ± 0.18 ps [48] and 6.2 ± 0.1 ps [49], respectively.

Of course, Quadra has a finite time resolution. We model this through a single Gaussian function with a width σ and expectation value Δ, which is convoluted with the sum of three exponential functions. The oPs lifetime τ_3 is therefore determined by fitting the following model to the TDD of a given VOI

$$F_\theta(t) \;=\; b + N \cdot \sum_{c=1}^{3} \frac{BR_c}{2\tau_c} e^{(\sigma^2 - 2t\tau_c + 2\Delta\,\tau_c)/(2\tau_c^2)} \cdot \mathrm{erfc}\Big(\frac{\sigma}{\sqrt{2}\tau_c} + \frac{\Delta - t}{\sqrt{2}\sigma}\Big)\,. \tag{3}$$

In Eq. (3), b denotes the background and N is a normalization constant. BR_c with $c = 1 \ldots 3$ and $\sum_c BR_c = 1$ are the relative branching ratios of pPs, direct annihilation and oPs, respectively. The θ stands for the collection of all fitting parameters, i.e.

$\tau_{1,2,3}$, $BR_{1,2,3}$, Δ, σ and N. We only consider time differences from $\Delta t_0 = -1.5$ ns to $\Delta t_{n+1} = 10$ ns for the parameter fitting.

As in Ref. [46], we rely on a Bayesian framework for the fitting procedure. From the parameters in Eq. (3) we fix the background b to the median value of the TDD with time differences smaller than -2 ns. All other parameters are sampled from prior distributions, which are mostly inspired by the values for water at 37°C reported in Ref. [54]. The priors for the lifetimes τ_c are

$$\begin{aligned} \tau_1 &\sim \mathcal{N}(0.14 \text{ ns}, 0.02 \text{ ns}) , \\ \tau_2 &\sim \mathcal{N}(0.39 \text{ ns}, 0.01 \text{ ns}) , \\ \tau_3 &\sim \mathcal{N}(1.78 \text{ ns}, 0.5 \text{ ns}) . \end{aligned} \tag{4}$$

Note that the fitted value of τ_1 from Ref. [54] differs from canonical $\tau_1 = 125$ ps (see e.g. Ref. [55]). This is likely due to the fact that the time it takes the positron to loose its energy prior to the pPs formation is not included in 125 ps. In any case, the prior of τ_1 in Eq. (4) includes the value of 125 ps within less than one standard deviation. For τ_3 we choose a rather wide and therefore uninformative prior distribution, which nevertheless accounts for our knowledge on the order of magnitude that we can expect in human tissue. The branching ratios of the three components follow a Dirichlet distribution, i.e.

$$BR_{1,2,3} \sim \text{Dirichlet}(0.75, 3.1, 1.15) . \tag{5}$$

The mean values of the distribution in Eq. (5) are 0.15, 0.62 and 0.23 and the standard deviations are 0.15, 0.20 and 0.17. Finally, the knowledge of Quadra's timing resolution allows us to set the prior distribution for σ and Δ to

$$\sigma \sim \mathcal{N}(0.1 \text{ ns}, 0.05 \text{ ns}) , \qquad \Delta \sim \mathcal{N}(0 \text{ ns}, 0.5 \text{ ns}) . \tag{6}$$

Finally, the normalization constant N is sampled from a normal prior distribution

$$N \sim \mathcal{N}(A, 0.1 \cdot A) \quad \text{with} \quad A = \int_{\Delta t_1}^{\Delta t_n} dt \; (y_i - b) . \tag{7}$$

y_i with $i = 1, \ldots, n$ are all observations in a TDD, i.e. the number of counts in a time difference bin i. The use of the factor A in Eq. (7), which is purely determined by the measured TDD, significantly stabilizes the numerical calculation.

The count statistics are sufficiently high that we can assume a Gaussian likelihood. All all observations y_i in a TDD are assumed to be independent and identically distributed (iid)

$$p(y|\theta) = \prod_{i=1}^{n} p(y_i|\theta) \quad \text{with} \quad p(y_i|\theta) \sim \mathcal{N}(F_\theta(\Delta t_i), \epsilon) . \tag{8}$$

Δt_i is the time difference of the bin i and the weakly informative prior on the variance ϵ^2 is the positive Cauchy-Lorentz distribution (see Ref. [56])

$$\epsilon \sim \text{Cauchy}^+(0, \sigma_b) , \tag{9}$$

where σ_b^2 is the variance of the background b and is determined, analogously to b itself, as a point estimate from the measured TDD.

The sampling of the posterior distributions $p(\theta|y)$ relies on a no-u-turn algorithm [57] and its implementation the software packages Julia [58], Turing.jl [59] and ArviZ [60]. We report our results in terms of expectation values and 68% highest density intervals (HDI). In most cases, the posterior distributions are bell-shaped and the use of the standard estimator for the variance would be meaningful. However, this does not need to be the case, in particular for BR_c, and we therefore stick to the HDI. The use of marginalized posterior distribution is particularly appealing since our main interest lies on the parameter τ_3 and all others can in principle be considered as nuisance parameters.

The afore described Bayesian fitting procedure applies to the parameter fitting to a TDD from a single VOI. A single VOI is drawn such that we can expect a similar tissue structure, and therefore similar oPs lifetime, throughout the whole VOI. However, oPs lifetime could on average be the same for different VOI, if we have reason to believe that the tissue structure is similar. The example we explored in this study is the oPs lifetime in arterial and venous blood. Conceptually, this requires a comparison of statistical models with different number of fitting parameters. E.g. let us suppose there are two VOI that contain mostly venous blood. The question we seek to answer is whether a model where τ_3 is sampled from one single distribution for the two VOI performs better than a model with two separate distributions for τ_3. Therefore, we construct hierarchical models (see e.g. Ref. [61]) and rely on a leave-one-out cross-validation (LOO-CV) according to Refs. [62–65].

Let us assume that we have $j = 1, \ldots, n_j$ different VOI. Each VOI has a TDD, which we shall denote as y_{ij} and a set of fitting parameters θ_j. The likelihood $p(y_j|\theta_j)$ is iid and factorizes as in Eq. (8). The fitting parameters θ_j are split into global parameters that are completely independent of the VOI and parameters that are VOI-dependent. $\tau_{1,2}$ are assumed to be independent of the tissue composition and the same applies to the scanner parameters σ and Δ. These parameters are sampled from a single prior distribution according Eqs. (4) and (6) and a sampled value is applied to all VOI. Next, the normalization N_j and statistical noise ϵ_j are specific to every single VOI. They are sampled from separate prior distributions, but with the same prior parameters as in Eqs. (7) and (9). Finally, the main feature of the hierarchical model is that we can assume that the oPs lifetime and branching ratios are sampled from a common distribution for multiple VOI. Fig. 2 shows the basic scheme of Bayesian hierarchical models used in this study. The likelihood remains the same as in Eq. (8), simply with an additional group (or VOI) index j. However, the prior distribution of $\tau_3^{(j)}$ and $BR_c^{(j)}$ is conditional on a series of hyperparameters, which we denote as ϕ. Specifically,

$$\begin{aligned} p(\tau_3^{(j)}|\mu_\tau, \sigma_\tau) &\sim \mathcal{N}(\mu_\tau, \sigma_\tau) \quad \text{for all} \quad j = 1, \ldots, n_j \ , \\ p(BR_c^{(j)}|\alpha_{BR}) &\sim \text{Dirichlet}(\alpha_{BR}) \quad \text{for all} \quad j = 1, \ldots, n_j \ , \end{aligned} \tag{10}$$

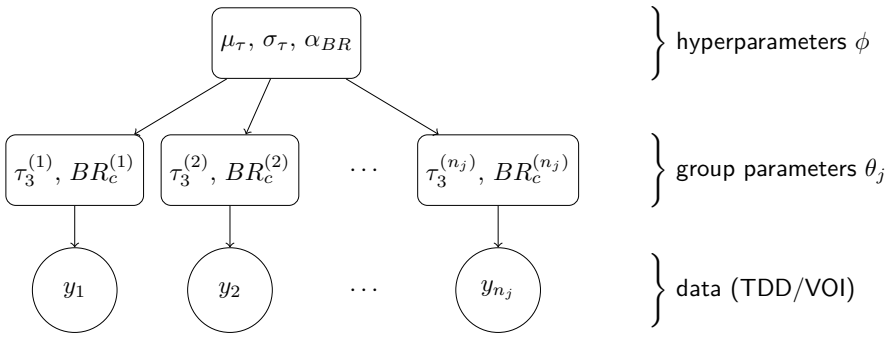

Fig. 2: Hierarchical model for the combined analysis of data from different VOI.

and the hyperparameters μ_τ, σ_τ, and α_{BR} are sampled from the following prior distributions

$$\begin{aligned} \mu_\tau &\sim \mathcal{N}(1.78 \text{ ns}, 0.5 \text{ ns}) \\ \sigma_\tau &\sim \text{Cauchy}^+(0, 0.5 \text{ ns}) \\ \alpha_{BR} &\sim \text{Dirichlet}(0.75, 3.1, 1.15) \end{aligned} \tag{11}$$

which reflect the priors in Eqs. (4) and (5).

Note that a basic assumption of Bayesian hierarchical models is that different VOI are exchangeable, i.e. the joint distribution $p(\theta_1 \ldots, \theta_{n_j})$ of the group-level parameters θ_j is invariant under permutation of the indices j. In our case, exchangeability is ensured by sampling independently from

$$p(\theta|\phi) \;=\; \prod_{j=1}^{n_j} p(\theta_j|\phi) \;. \tag{12}$$

We allow also for partial exchangeability. In some cases, we have prior knowledge and we can form subgroups of VOI and each subgroup has its own exchangeable hierarchical model with a common population distribution. More specifically, let us assume that the first s_j VOI belong to a subgroup, then the permutation invariance applies to the sets of indices $j = 1, \ldots, s_j$ and $j = s_j + 1, \ldots, n_j$ separately. The joint posterior distribution for θ and ϕ is

$$p(\theta, \phi|y) \;\propto\; p(\theta, \phi) \cdot p(y|\theta, \phi) \;=\; p(\phi) \prod_{j=1}^{n_j} p(\theta_j|\phi) \cdot p(y_j|\theta_j) \;, \tag{13}$$

where the priors $p(\phi)$ are given in Eq. (11) and the conditional distribution $p(\theta_j|\phi)$ is simply a short-hand notation for the distributions in Eq. (10). Note that $p(\theta, \phi|y)$ does not factorize.

In the present study, we construct hierarchical models for VOI of subject S3 containing venous and arterial blood. The working hypothesis is that the lower oxygen content of venous blood compared to arterial blood is reflected in a through different

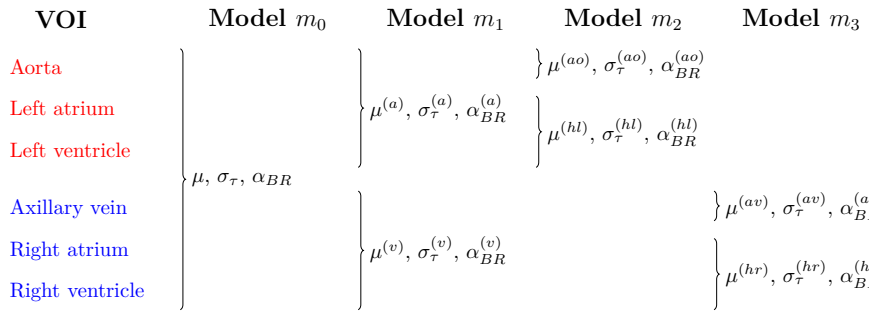

Fig. 3: Hierarchical models for the comparison of oPs lifetimes in VOI with venous (blue) or arterial blood (red).

oPs lifetimes. We set up four different hierarchical models, as shown schematically in Fig. 3. In model m_0 the oPs lifetime is sampled from a common distribution for all six VOI under consideration (aorta, left atrium and ventricle, axillary vein, right atrium and ventricle). For model m_1 we separate two subgroups of three VOI each according to their blood content. This means that the three oPs lifetimes $\tau_3^{(a,v)}$ and branching ratios $BR_v^{(a,v)}$ of the VOI inside one subgroup are sampled form a common population distribution. This population distribution is different for the arterial (index a) and venous blood (index v) subgroups. Lastly, in model 2 and 3 we combine the heart chambers and compare them with the axillary vein or aorta. For these two models, the fit data encompasses only three TDD.

The interesting aspect of this analysis is, of course, to compare the performance of the different hierarchical models, even if the number of fitting parameters is different. We evaluate the hierarchical models in Fig. 3 according to their out-of-sample predictive accuracy while taking into account the uncertainty of its estimate. LOO-CV in combination with a Pareto smoothed importance sampling is a robust and efficient approach for estimating the out-of-sample predictive accuracy without refitting the model (see Ref. [62, 63]).

The basic idea behind LOO-CV is to find an approximation for the the expected log pointwise predictive density elpd for $i = 1, \ldots, \tilde{n}$ new data points $\tilde{y}_i$ given the data generating model m and the data y. The elpd is

$$\mathrm{elpd}(m|y) \;=\; \sum_{i=1}^{\tilde{n}} \int d\tilde{y}_i \; p_t(\tilde{y}_i) \cdot \log\left(p_m(\tilde{y}_i|y)\right) \;. \tag{14}$$

$p_t(\tilde{y}_i)$ is the true distribution for generating new data (and the observed data y as well) and is therefore unknown. For a hierarchical model m, the posterior predictive density $p_m(\tilde{y}_i|y)$ for new data is the marginalized distribution

$$p_m(\tilde{y}_i|y) = \int d\tilde{\theta}\, d\phi \; p(\tilde{y}_i|\tilde{\theta}) \cdot p(\tilde{\theta}|y,\phi) \cdot p(\phi|y) \;. \tag{15}$$

where $\tilde{\theta}$ are new group-level parameters for the data $\tilde{y}$. In the absence of independent validation data, we can use LOO-CV to estimate elpd

$$\mathrm{elpd}_{LOO}(m|y) \;=\; \sum_{i=1}^{n} \log\left(p_m(y_i|y_{-i})\right) \;, \tag{16}$$

where y_{-i} are all observations in y except y_i and predictive density $p_m(y_i|y_{-i})$ is analogous to Eq. (15). The Pareto smoothing importance sampling from Ref. [63] stabilizes the weights when computing $\mathrm{elpd}_{LOO}(m|y)$ and allows for a robust estimate of the variance.

In order to compare two different models m_a and m_b from Fig. 3, we can simply evaluate the sign of the edlp difference

$$\Delta\mathrm{elpd}(m_a, m_b|y) \;=\; \mathrm{elpd}_{LOO}(m_a|y) - \mathrm{elpd}_{LOO}(m_b|y) \;. \tag{17}$$

3 Results

First, we present in Fig. 4 the histoimages of all detected 3γE of the three subjects. For each count in Fig. 4 we are able to determine a time difference between the prompt and the annihilation photons. The voxel size is chosen according to the CT image, i.e. $0.98 \times 0.98 \times 3.0\,\mathrm{mm}$ for S1, $1.52 \times 1.52 \times 3.0\,\mathrm{mm}^3$ for S2 and $1.52 \times 1.52 \times 1.65\,\mathrm{mm}^3$ for S3. These histoimages resemble typical distribution of the radiopharmaceuticals administered to the three subjects, i.e. there is a prominent uptake of [^{68}Ga]Ga-DOTA-TOC in S1's meningioma and spleen, the clearly visible parotid glands of S2 and the well perfused heart, kidneys and right veins through with the ^{82}Rb was injected into S3. This, of course, correlates well with the coincidence PET images shown in Fig. 1. It is important to note that the histoimages in Fig. 4 contain all 3γE, including background and random three-photon coincidences. The maximum voxel values in the histoimages are 476 counts in S1's meningioma, 1591 counts in S2' kidneys and 1147 counts in the right median cubital vein of S3.

The main results of this study are the TDDs of selected VOIs that are shown in Figs. 5, 6 and 7 for the three subjects. The error bars shown in these TDD are the relative standard deviation of the background regions with $\Delta t < -2$ ns. The noise level for different organs varies quite a bit. The relative error in the background region ranges from 0.2 % for S2's liver to 4.6 % for S3's thyroid.

Fig. 8 illustrates the difference of the peak-normalized TDD for selected organs across the three subjects. While the count statistics for S1 and S2 are much higher (see the MIP in Fig. 4), the peak signal-to-background ratio (pSBR) is significantly higher for S3. Despite having low statistical noise, as seen e.g. in the liver of S1 and S2, the pSBR does not go beyond ≈ 1.3. On the other hand, for S3 we found that pSBR is consistently above ≈ 3.3 for the VOI under consideration.

From the measured TDD we can determine the oPs lifetime through the Bayesian fitting procedure described in Sec. 2.3. For the VOI with decent count statistics and SBR, Tabs. 4, 5 and 6 report the fitted oPs lifetimes and branching ratios of the three fit components (pPs, direct annihilation and oPs). The HDI are taken at 68%. Note

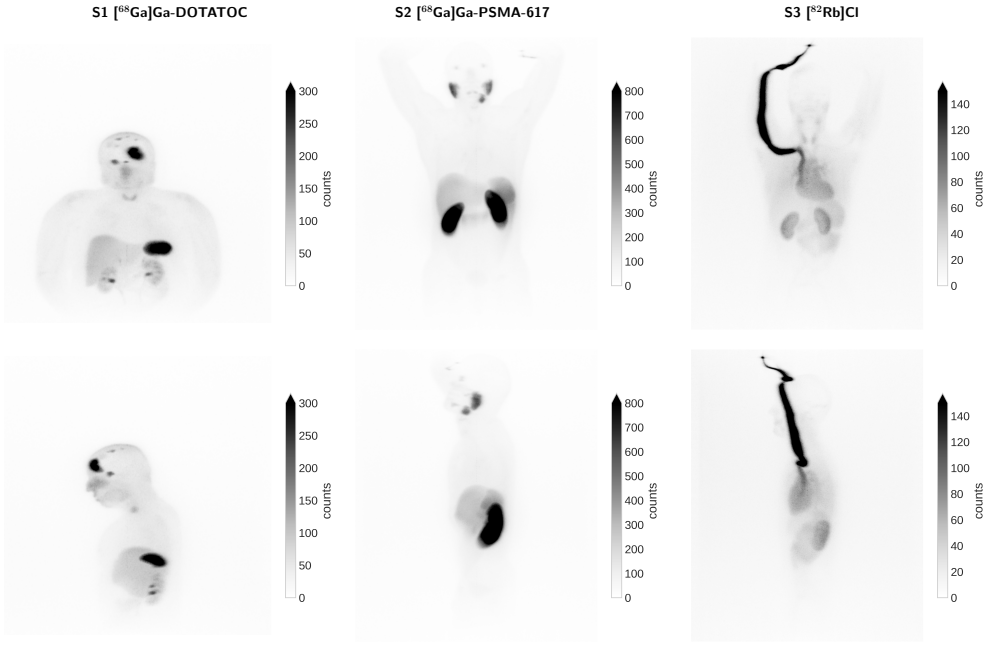

Fig. 4: Coronal (top row) and sagittal (bottom row) MIP of the histoimages for the subjects S1 (left), S2 (center) and S3 (right). These MIP of the histoimages resemble typical coincidence PET images for these tracers. Note that the histoimages include all detected 3γE, i.e. also the background events.

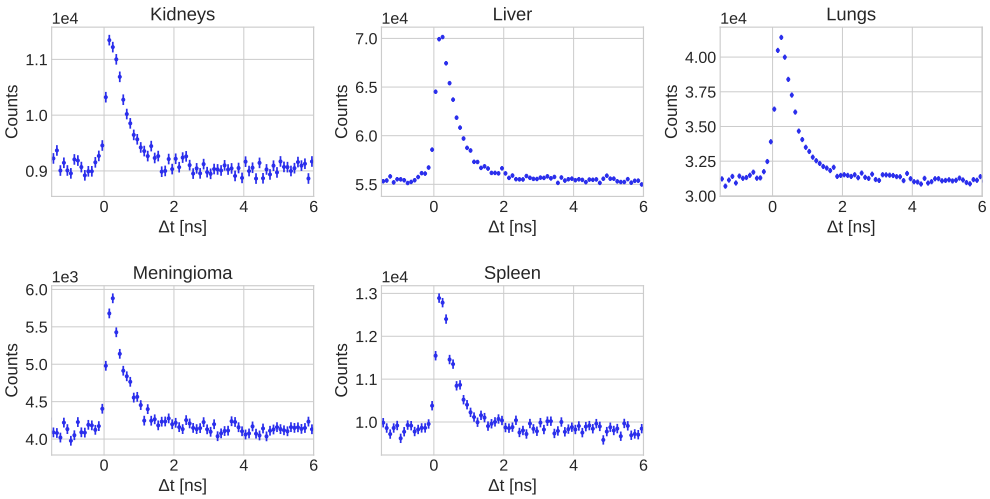

Fig. 5: Measured TDD for selected VOI from subject S1.

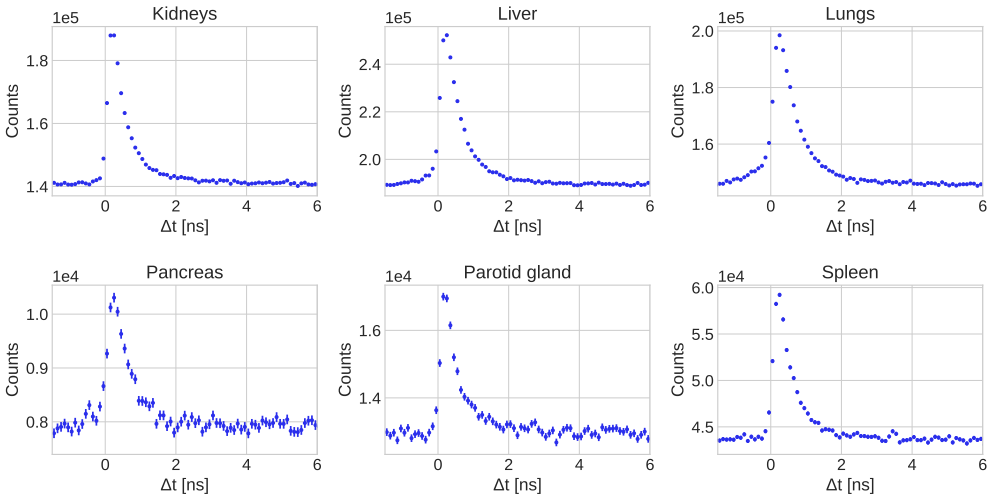

Fig. 6: Measured TDD for selected VOI from subject S2.

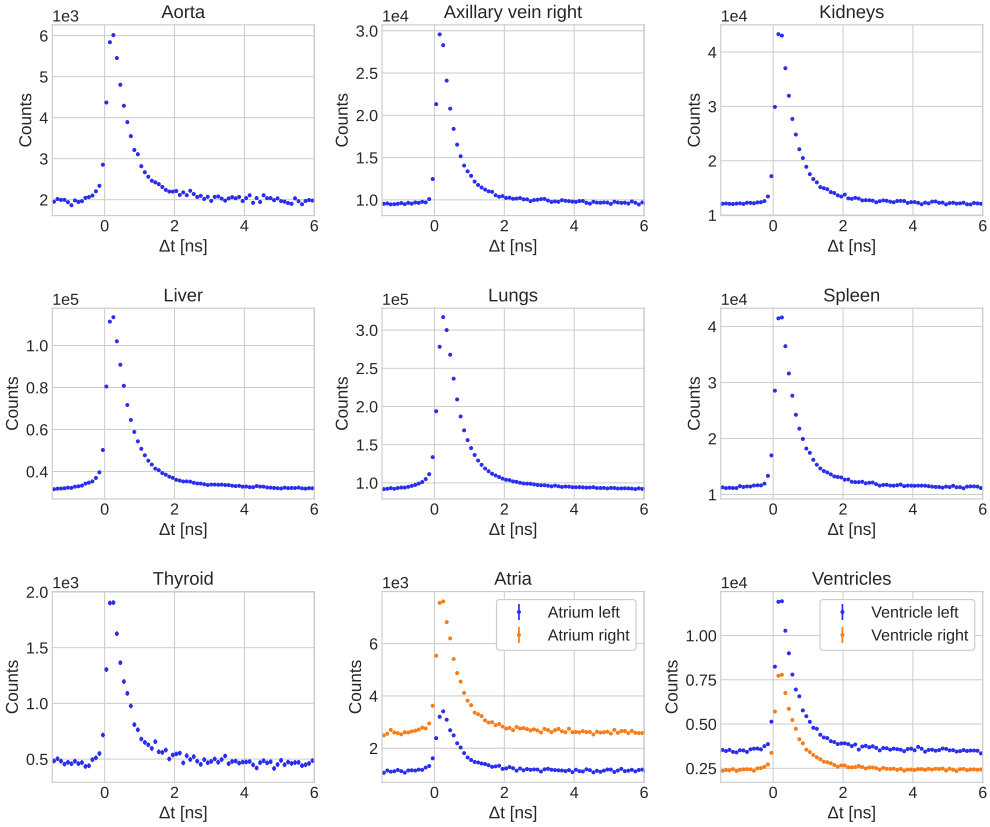

Fig. 7: Measured TDD for selected VOI from subject S3.

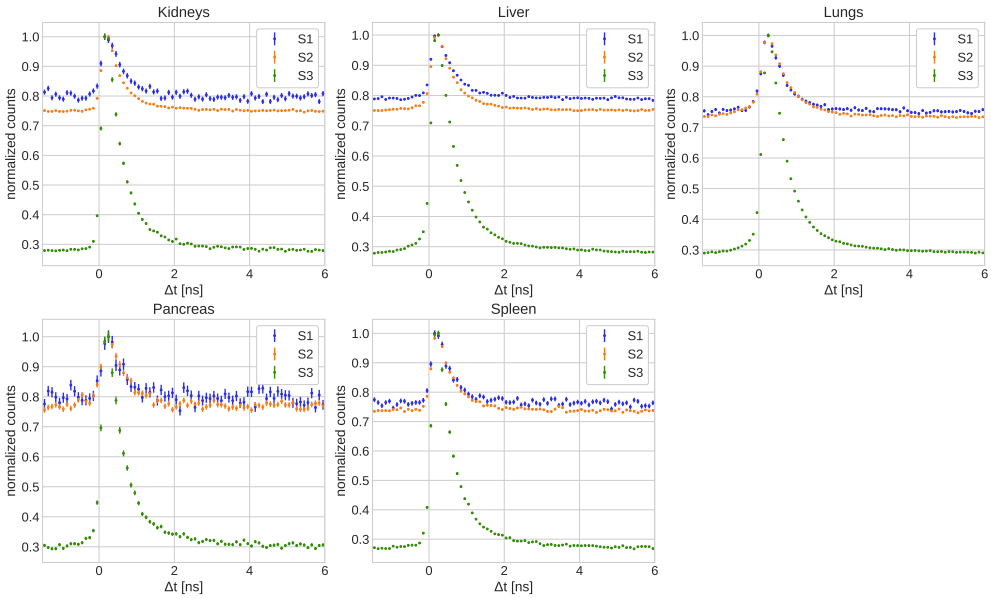

Fig. 8: Comparison of organ TDD from the three subjects.

Table 4: Fit results for selected organs from S1.

VOI	τ_3 [ns]	HDI_{τ_3} [ns]	BR_1	HDI_{BR_1}	BR_2	HDI_{BR_2}	BR_3	HDI_{BR_3}
Kidneys	1.65	[1.12, 2.2]	0.08	[0.0, 0.06]	0.71	[0.68, 0.89]	0.21	[0.10, 0.26]
Liver	1.92	[1.52, 2.28]	0.02	[0.0, 0.02]	0.73	[0.71, 0.78]	0.25	[0.22, 0.28]
Lungs	1.98	[1.62, 2.28]	0.07	[0.0, 0.09]	0.66	[0.61, 0.74]	0.28	[0.24, 0.3]
Meningioma	1.58	[1.10, 1.94]	0.06	[0.0, 0.08]	0.67	[0.60, 0.78]	0.27	[0.20, 0.32]
Spleen	2.29	[1.89, 2.66]	0.11	[0.05, 0.16]	0.59	[0.51, 0.68]	0.30	[0.26, 0.34]

that the posterior distribution of τ_3 is mostly bell-shaped and it would therefore also make sense to estimate the posterior variance through the common point estimate. However, the posterior distributions of BR_c are far from being bell-shaped. Estimating a variance would be meaningless. As expected, the high pSBR leads to considerable uncertainty on τ_3 for S1. While the first moment of τ_3's posterior distribution shifts compared to the prior in Eq. (4), the HDI is only slightly smaller than the prior's. Except for the pancreas, the VOI of S2 give already a reasonable constrain on τ_3. In line with expectations, Tab. 6 shows that S3's TDD are most constraining on the posterior distributions of τ_3 and BR_c.

Fig. 9 depicts the fitted values for τ_3 from Tabs. 4, 5 and 6. The error bars are the 68% HDI_{τ_3}. As a comparison, we added the results for the oPs lifetime of the glioblastoma and parotid gland from Ref. [30]. For these two data points, the error bars are the standard deviation from Ref. [30]'s frequentist fit. The fit predictions are visualized in Fig. 10. For the most interesting VOI we show the measured TDD

Table 5: Fit results for selected organs from S2.

VOI	τ_3 [ns]	HDI_{τ_3} [ns]	BR_1	HDI_{BR_1}	BR_2	HDI_{BR_2}	BR_3	HDI_{BR_3}
Kidneys	1.70	[1.50, 1.86]	0.11	[0.08, 0.13]	0.63	[0.6, 0.66]	0.26	[0.24, 0.28]
Liver	1.46	[1.16, 1.68]	0.04	[0.0, 0.05]	0.7	[0.67, 0.77]	0.26	[0.22, 0.28]
Lungs	1.35	[1.00, 1.57]	0.05	[0.0, 0.06]	0.61	[0.56, 0.72]	0.34	[0.27, 0.38]
Pancreas	1.59	[1.07, 2.06]	0.05	[0.0, 0.06]	0.77	[0.71, 0.88]	0.18	[0.11, 0.24]
Parotid gland	1.49	[1.04, 1.76]	0.18	[0.13, 0.24]	0.52	[0.42, 0.64]	0.30	[0.23, 0.35]
Spleen	1.63	[1.28, 1.89]	0.07	[0.03, 0.1]	0.69	[0.64, 0.76]	0.24	[0.21, 0.27]

Table 6: Fit results for selected organs from S3.

VOI	τ_3 [ns]	HDI_{τ_3} [ns]	BR_1	HDI_{BR_1}	BR_2	HDI_{BR_2}	BR_3	HDI_{BR_3}
Aorta	1.60	[1.34, 1.80]	0.02	[0.0, 0.02]	0.67	[0.65, 0.72]	0.31	[0.28, 0.33]
Axillary vein	1.80	[1.66, 1.94]	0.09	[0.08, 0.1]	0.66	[0.64, 0.68]	0.26	[0.24, 0.27]
Kidneys	1.72	[1.55, 1.86]	0.04	[0.02, 0.06]	0.70	[0.68, 0.72]	0.26	[0.25, 0.28]
Liver	1.44	[1.25, 1.58]	0.01	[0.0, 0.01]	0.64	[0.61, 0.68]	0.35	[0.32, 0.38]
Lungs	1.52	[1.32, 1.66]	0.02	[0.0, 0.03]	0.67	[0.65, 0.71]	0.31	[0.28, 0.33]
Spleen	1.66	[1.48, 1.80]	0.03	[0.0, 0.03]	0.69	[0.66, 0.72]	0.29	[0.27, 0.30]
Thyroid	1.83	[1.51, 2.08]	0.04	[0.0, 0.05]	0.69	[0.65, 0.74]	0.28	[0.24, 0.30]
Atrium left	1.50	[1.15, 1.72]	0.02	[0.0, 0.03]	0.71	[0.68, 0.77]	0.26	[0.22, 0.29]
Atrium right	1.76	[1.46, 1.99]	0.01	[0.0, 0.01]	0.72	[0.7, 0.75]	0.27	[0.24, 0.29]
Ventricle left	1.44	[1.22, 1.60]	0.04	[0.02, 0.07]	0.67	[0.63, 0.72]	0.29	[0.26, 0.31]
Ventricle right	1.96	[1.69, 2.18]	0.02	[0.0, 0.02]	0.72	[0.7, 0.75]	0.26	[0.24, 0.28]

Table 7: Fit results for the ^{82}Rb and ^{124}I blood samples. The starred venous blood sample was measured with [^{82}Rb]Cl.

Sample	τ_3 [ns]	HDI_{τ_3} [ns]	BR_1	HDI_{BR_1}	BR_2	HDI_{BR_2}	BR_2	HDI_{BR_3}
Venous*	1.85	[1.79, 1.91]	0.09	[0.08, 0.09]	0.70	[0.69, 0.71]	0.21	[0.21, 0.22]
Venous	1.80	[1.48, 2.04]	0.06	[0.02, 0.08]	0.71	[0.67, 0.76]	0.24	[0.21, 0.26]
Arterial	1.78	[1.71, 1.84]	0.08	[0.07, 0.09]	0.69	[0.68, 0.7]	0.23	[0.22, 0.23]
Water	1.77	[1.74, 1.80]	0.10	[0.09, 0.11]	0.62	[0.62, 0.62]	0.28	[0.28, 0.28]

together with the posterior mean for the three fit components and their sum. Note that the fit ranges from −1.5 ns to 8 ns. The limit of 6 ns in Fig. 10 is selected purely for improved visualization.

Fig. 12 shows the picture of the ^{124}I experiment with the coincidence PET and the 3γE image. The fit results can be found in Tab. 7. The oPs lifetime seems to be very similar in all three samples. Fig. 12 depicts the posterior mean prediction for three samples and the measured TDD. The pSBR of the three samples is 37.26 for the venous blood, 42.98 for the arterial blood and 37.29 for the water sample. This is almost one order of magnitude more compared to the pSBR from the ^{68}Ga and ^{82}Rb scans, despite the relatively short scan time of 15 min.

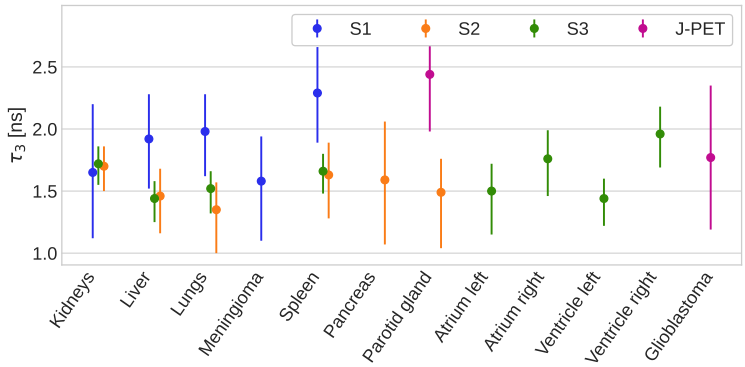

Fig. 9: Visualization of the fitted values of τ_3 for the three subjects and comparison with the oPs lifetime of the glioblastoma and pituitary glands in Ref. [30].

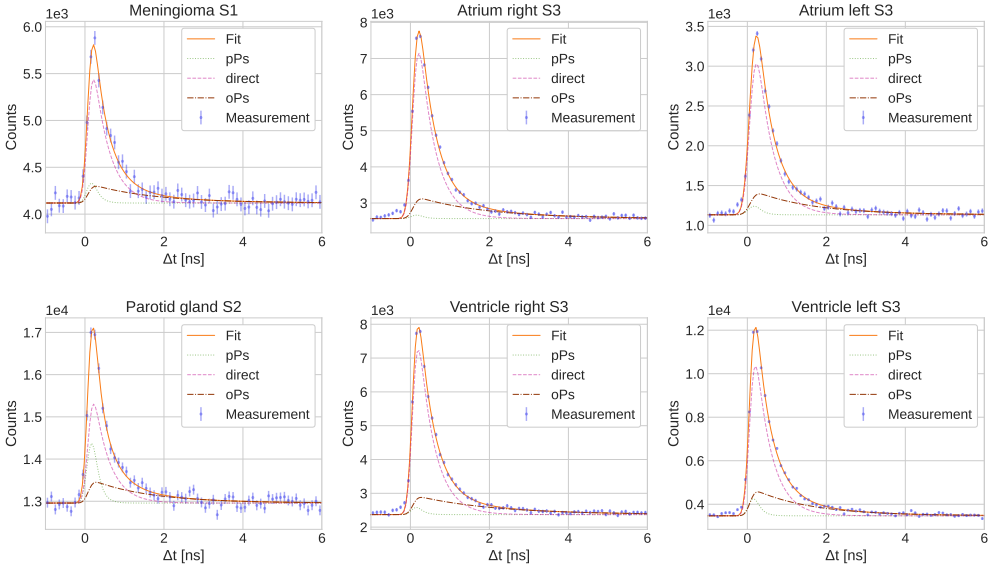

Fig. 10: TDD and fit prediction (posterior mean) for selected VOI.

The hierarchical models from Fig. 3 are fitted to the aorta, the right axillary vein, the ventricles and the atria of S3 and we report the results in Tab. 8. The posterior distribution for σ_τ is strongly skewed and truncated at 0. Therefore, we only quote the 68% HDI for these hyperparameters.

The 68% HDI_{μ_τ} of $\mu_\tau^{(a,v)}$ of m_1 in Tab. 8 overlap slightly, but the expectation value of the arterial blood VOI $\mu_\tau^{(a)}$ is almost 0.4 ns lower than for the arterial blood. If we were to fix both $\tau_{1,2}$ in the hierarchical model fit, the two HDI_{μ_τ} would not overlap, i.e. $\mu_\tau^{(a,v)}$ would tend to lower values and the HDI_{μ_τ} would be $[1.10, 1.45]$ ns

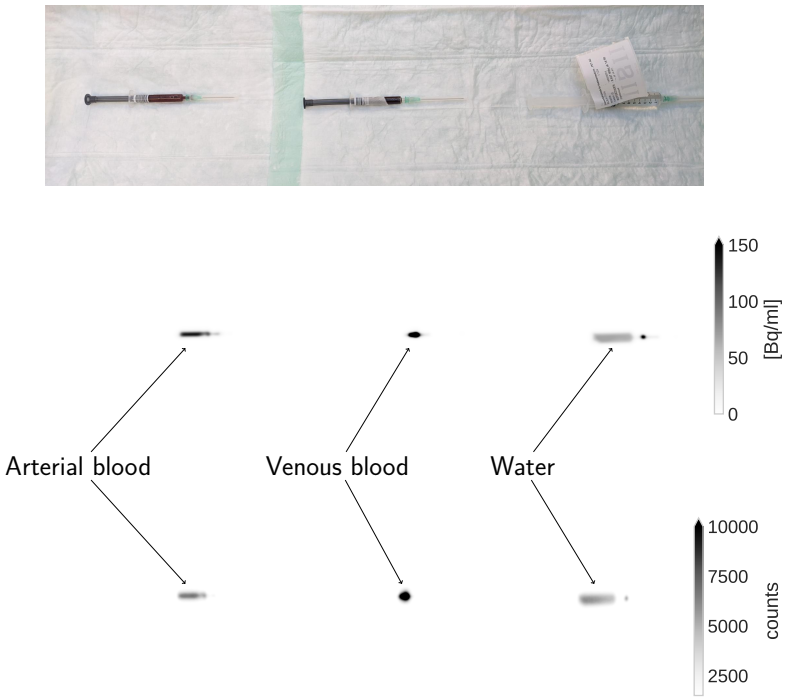

Fig. 11: Picture of the ^{124}I blood samples and water lying on Quadra's patient bed (top) together with the MIP of the coincidence PET image (middle) and 3γE histoimage (bottom).

and $[1.49, 1.81]$. the HDI for both $\mu_\tau^{(a)}$ and $\mu_\tau^{(v)}$ are significantly smaller than the HDI of the prior distributions in Eq. (11), meaning that the measured TDD are strongly constraining the hyperparameters. Fig. 13 shows the posterior distribution of the hyperparameters in the models $m_{0,1}$. When comparing the elpd$_{LOO}$ of the two models $m_{0,1}$, we notice only a slight improvement for m_1, i.e. $\Delta\text{elpd}(m_0, m_1|y) < 0$. The difference is, however, much smaller than the estimated standard error of elpd$_{LOO}$ quoted in the last column of Tab. 8. When comparing the hyperparameters of model m_2 in Tab. 8, it seems that $\mu_\tau^{(ao)}$ approaches higher values (similar to water), while the left heart chambers seem to drive the oPs lifetime to smaller values. In model m_3 however, τ_3 in the right axillary vein is in line with the one in the right heart chambers.

4 Discussion

In Ref. [46] we showed that the measurement of oPs lifetime is feasible with Quadra and that our methodology is able to reproduce well-established results from the literature. In this study we report three in vivo measurements of oPs lifetime with Quadra. It is remarkable that the selection of 3γE and the determination the time difference

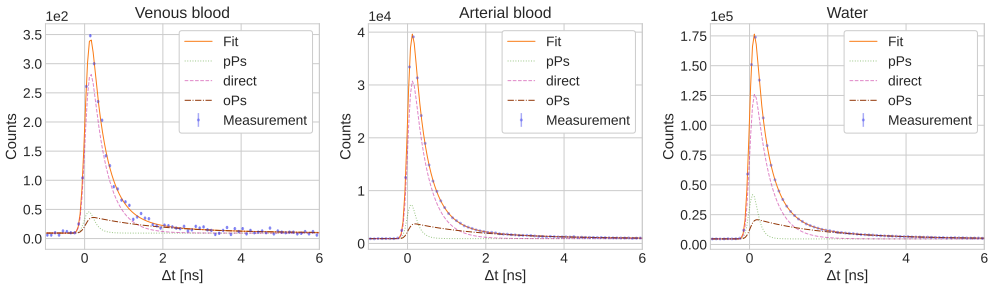

Fig. 12: TDD and fit prediction for the three ^{124}I samples.

Table 8: Fit results for the hyperparameters in the hierarchical models from Fig. 3 together with the LOO estimate of elpd_{LOO} and its standard error.

Model	μ_τ [ns]	HDI_{μ_τ} [ns]	HDI_σ	BR_3	HDI_{BR_3}	elpd_{LOO}	$\text{se}(\text{elpd}_{LOO})$
m_0	1.84	[1.66, 2.0]	[0.01, 0.25]	0.33	[0.22, 0.42]	-3211.73	36.62
$m_1^{(a)}$	1.62	[1.4, 1.84]	[0.01, 0.3]	0.32	[0.18, 0.43]	-3211.95	36.4
$m_1^{(v)}$	2.0	[1.78, 2.21]	[0.0, 0.27]	0.3	[0.17, 0.4]		
$m_2^{(ao)}$	1.75	[1.41, 2.07]	[0.0, 0.51]	0.29	[0.1, 0.41]	-1556.17	23.1
$m_2^{(hl)}$	1.48	[1.2, 1.68]	[0.01, 0.33]	0.3	[0.15, 0.42]		
$m_3^{(av)}$	1.86	[1.59, 2.14]	[0.0, 0.47]	0.26	[0.08, 0.35]	-1640.49	22.03
$m_3^{(hr)}$	1.85	[1.54, 2.13]	[0.01, 0.46]	0.31	[0.14, 0.41]		

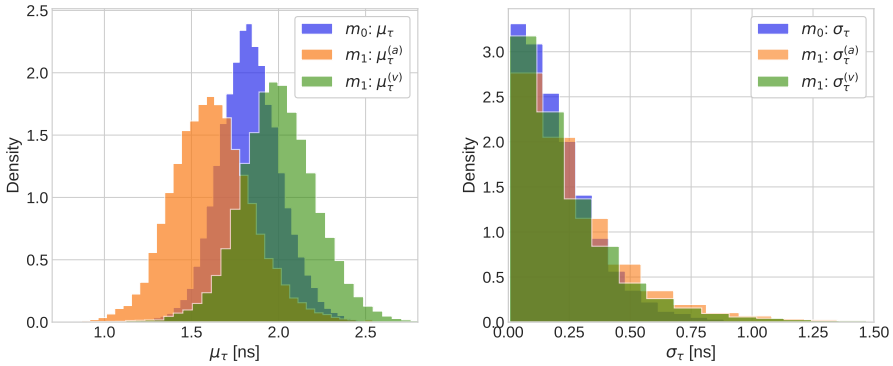

Fig. 13: Comparison between the sampled posterior distributions of the hyperparameters of the models m_0 and m_1 (see Fig. 3).

between the prompt and annihilation photon is possible on a commercial medical device. We hope that our results can brake the ground for further investigations and developments of PALS in medical applications. A first in vivo oPs lifetime measurement was previously presented in Ref. [30]. However, the scanner use in the mentioned work is a dedicated prototype scanner with a standard FOV and is not commercially available. The J-PET measurement is plagued by low count statistics. Simulations in

Ref. [66] suggested that Quadra's sensitivity is about 400 times higher than J-PET's. Figs. 5, 6 and 7 do not suggest such a large difference between the two scanners, but there is no denial that Quadra outperforms the current version of the J-PET scanner with respect to count statistics. Note, however, that the pSBR in Fig. 3 of Ref. [30] is at least ≈ 9. Likely, this is due to the difference in Quadra's and J-PET's detector materials and energy range as well as in the event selection procedures. The scaling relation of Quadra's sensitivity with the axial length of a PET scanner discussed in Ref. [30] is therefore too optimistic and does not take into account different event selection procedures. We leave a thorough comparison of the two systems' performance for PALS measurements to future studies.

However, also for Quadra and the present study the count statistics of 3γE is the main issue. As seen in Fig. 8, the pSBR is significantly lower for the ^{68}Ga-based compounds compared to ^{82}Rb and the background noise is typically higher. The lower prompt photon branching ratio of ^{68}Ga (see Tab. 2) and the longer scan times for S1 and S2 increase random 3γE and therefore the background in the measured TDD. On the other hand, [^{82}Rb]Cl has only a marginal uptake in any tissue due to the large decay constant. This means that oPs lifetime in S3 is likely to reflect the properties of blood and not of the tissue that takes up the tracer. In view of additional diagnostic information through PALS measurements, this makes [^{82}Rb]Cl less interesting. In our opinion, future in vivo PALS studies with Quadra should focus on ^{124}I. The prompt photon branching ratio is substantially higher compared to ^{68}Ga and ^{82}Rb and Quadra is able to fully resolve the ^{124}I photopeak at 602.73 keV (see Ref. [46]). From the clinical perspective, standardized uptake values (SUV) for ^{124}I are typically very high and it is known that tumor differentiation in thyroid cancer patients depends on tumor hypoxia (see e.g. Ref. [67]). Being able to measure tumor oxygenation levels thorough the oPs lifetime could provide an important diagnostic information for thyroid cancer patients. Radionuclides like ^{44}Sc, ^{89}Zr or $^{52m/52g}$Mn have prompt photon branching ratio around 100% or more. However, it is not clear how much the count statistics would improve since Quadra is not able to resolve the photopeak for these radionuclides. Depending on the tracer, count statistics for in vivo PALS measurements might also be plagued by low SUV, as e.g. in the case of immuno-PET with ^{89}Zr.

The fitting function in Eq. (3) inherently induces strong correlations, in particular among the Gaussian parameters σ and Δ as well as among each τ_i and the corresponding BR_c (see the pair plot in Fig. 15 of Ref. [46]). Having a low noise and background level is therefore crucial for disentangling these correlations and to limit the uncertainties in the marginalized posterior distributions. As should be clear from the discussion in Sec. 2.3, we take a rather conservative approach to the TDD fitting procedure. From the parameters in Eq. (3), we only fix the TDD's background b. Through our event selection procedure, the TDD contains random 3γE with negative time differences. As shown in Ref. [46] with ^{18}F measurements, the crystal distance threshold in the event selection gives a flat background throughout positive and negative time differences. We are therefore confident that estimating b from events with negative time differences yields an accurate estimate. Note that allowing for b to be a fit parameter would introduce a strong correlation with τ_3 since oPs is dominant in tail region of

the TDD (starting at around 2 ns). For the background estimation, Ref. [30] takes a similar approach. The priors on $\tau_{1,2}$ in Eq. (4) are quite narrow, reflecting our strong prior knowledge on these times and their independence from the surrounding material. Despite this strong prior we allow for a variation of $\tau_{1,2}$ and keep from fixing these values. As shown e.g. in Refs. [54, 68] measurements of $\tau_{1,2}$ do show some variation across different measurements. The rather uninformative prior on τ_3 expresses our lack of prior knowledge about oPs lifetimes in tissue. The same applies to the priors on BR_c. Also the 50% error on Quadra's timing resolution parameter σ in Eq. (6) is conservative. Note that the noise does not really follow a Poisson distribution. A quick check with a quantile-quantile plot reveals that for all VOI the background noise is mostly normal distributed. The choice of likelihood in Eq. 8 is therefore justified.

Other research groups have made approximations to reduce the uncertainty on τ_3 if the TDD's count statistics is low. In Ref. [55] the J-PET collaboration fixes the pPs lifetime τ_1 and direct annihilation time τ_2. Ref. [44] relies on a two-component model, i.e. one short- and one long-lived. The lifetime of the long-lived component is then quoted as the oPs lifetime. The authors of Ref. [30] go even further by fixing the branching ratios of a two-component model, effectively leaving only τ_3 and a scale parameter as a free parameters. In our view, these approaches limit the interpretability of the longer lived component as being oPs in a physical sense and may limit the possibility to compare with in vitro PALS measurements. When comparing the fitted oPs lifetimes from J-PET with our HDI_{τ_3} in Fig. 9, it is important to consider the differences in event selection and fitting methodologies.

We refrain from determining τ_3 at the voxel level for the three subjects in our study. Such a Ps lifetime image is not feasible with the current level of count statistics, with our fitting methodology and a reasonably small voxel size. For S3, with a clinically irrelevant voxel size of $34.8 \times 34.9 \times 22.1\,\mathrm{mm}^3$, the TDD pSBR exceeds ≈ 3 and background noise drops below 6%, but only for voxels above the 95% quantile in accumulated 3γE. The authors of Ref. [55] showed that the modular J-PET detector is capable of collecting enough statistics for Ps lifetime imaging in tissue samples using a ^{22}Na source, though with a relatively large voxel size of $2 \times 2 \times 2\,\mathrm{cm}^3$.

In general, the oPs lifetimes shown in Tabs. 4, 5 and 6 are of the same order of magnitude as in water. At 37° water temperature, Ref. [54] reports $\tau_3 \approx 1.78$ ns, but there are also slightly higher values reported in the literature (see e.g. Ref. [69]). We refer the reader to Ref. [11] for a discussion on the difficulty to interpret the temperature dependence of oPs lifetimes. This makes the comparison of ex vivo and in vivo PALS measurements challenging, in particular if the precision in the latter will improve in the future. In general, it is fair to say that at this point we lack an interpretation for the fitted τ_3 values. Only future large scale in vitro, preclinical and clinical PALS measurements will eventually allow for a rigorous interpretation of τ_3 as a biomarker. In this vein, our study is merely showing what commercial PET systems are capable of and what the current challenges for in vivo PALS measurements are.

The HDI_{τ_3} in Tabs. 4, 5 and 6 are consistently smaller the width of τ_3's prior distribution. This means that the data is constraining the posterior distribution and can therefore provide a gain in information. From Figs. 5, 6 and 7 it is clear that the

oPs contribution becomes dominant only for time differences $\gtrsim 2$ ns. This is merely the consequence of the orders of magnitude of τ_i and BR_c.

The τ_3 values of S1 in Tab. 4 are plagued by a rather large HDI_{τ_3}. This is a consequence of the low pSBR. The most interesting VOI of S1 is certainly the meningioma. A Gd-enhanced MR scan prior to the PET scan showed a good perfusion of the meningioma and also the coincidence PET image does not show any larger areas without uptake. A τ_3-increasing hypoxia is therefore not to be expected which corroborates, well with the lower expectation value oPs lifetime in Tab. 4.

It seems that for S1 the spleen tends to higher oPs liftimes. This is somewhat in contrast to the value measured in S2's spleen in Tab. 5. Also in the lungs we find a mild discrepancy when comparing S1 with S2: while S2 seems to favor shorter τ_3, S1 shows a longer oPs lifetime. Given the large uncertainties and the multiple different structures in a lung, we refrain from over interpreting this difference.

The increased count statistics for S2 compared to S1 translate into smaller HD_{τ_3}. We were able to improve S2's count statistics through the increased singles scan time and different tracer kinetics (e.g. [^{68}Ga]Ga-PSMA-617 is taken up in the kidneys while [^{68}Ga]Ga-DOTA-TOC is merely excreted through the kidneys).

Since [^{82}Rb]Cl is a perfusion tracer, we expect the oPs lifetimes listed in Tab. 6 to be mostly driven by the molecular structure of the blood's constituents. The meta-analysis in Ref. [70] found an average difference of 4.92 ± 0.61 kPa in partial pressure of oxygen $P_{a,v}O_2$ between venous and arterial blood. In conjunction with the results of Ref. [23], there is the potential to measure the $P_{a,v}O_2$ through oPs lifetime measured in S3. Considering the VOI in Tab. 6 that contain arterial or venous blood, the expectation values for τ_3 seem to be consistently lower for arterial blood. However, the HDI_{τ_3} of the left and right heart chambers overlap, making these differences non-significant. We tried to see if the effect in the left and right heart chambers is reproducible in arterial and venous blood samples from S3. As shown in Tab. 7, we are not able to find a significant difference in oPs lifetime in the two blood types. Two venous blood samples are consistent, despite the different additional volumes from the radioactive source and the different time between sampling and singles mode scan. The oPs lifetime in the arterial blood sample is unexpectedly high. We believe, however, that this result is strongly affected by the sample preparation. As shown e.g. in Ref. [71] P_aO_2 can change by more than 10% within 15 min after taking the sample. In our case the sample preparation took about 25 min and the singles mode scan lasted for additional 15 min. We should therefore not expect P_aO_2 in the arterial blood sample to be comparable with P_aO_2 in S3's left heart chambers and aorta.

Given the Bayesian framework we are using, it is easy to go beyond a mere comparison of single VOI fit values to investigate the oPs lifetime in the heart chambers of S3. In fact, we believe that hierarchical models are one of the most effective ways to approach grouping data from different entities. As was the case for the single VOI fits in Tab. 6, the hyperparameters' HDI_{μ_τ} of the posterior distributions are smaller compared to the priors. However, HDI_{μ_τ} in Tab. 8 is comparable to HDI_{τ_3} in Tab. 6. This could be interpreted in two ways: on one hand, the two-level hierarchical model is too complex for the information can be gained from the grouping of VOI. On the other hand, it is remarkable that we are able to actually constrain $\mu_\tau^{(a)}$ and $\mu_\tau^{(v)}$ in m_1.

The two models m_0 and m_1 only marginally differ in their elpd and therefore perform very similarly on the data we have at our disposal. At this point we have to conclude that we are not sensitive enough to correlate oxygenation levels in arterial and venous blood with oPs lifetimes. Even fixing some of the fit parameters does not significantly improve the difference of $\mu_\tau^{(a)}$ and $\mu_\tau^{(v)}$. Adapting an approach to the τ_3 fitting in S3 that is more in line with Refs. [30, 55] might allow for a stronger statement. We leave this question open for future studies to answer.

5 Conclusions

In this study, we demonstrated the feasibility of performing in vivo oPs lifetime measurements using a commercial LAFOV PET/CT. With [^{82}Rb]Cl, organ-level oPs lifetime can be determined with reasonable statistical uncertainty, though SBR remains a challenge, particularly for ^{68}Ga and voxel-level τ_3 measurements. We hope that our findings pave the way for new applications in nuclear medicine and help encourage further human studies on a larger scale.

Acknowledgements. We would like to thank Janneke Henniphof, Angela Mendes and Silvia Tschopp for their help with the blood sample measurements.

Declarations

Funding. This research is partially supported by the grant no. 216944 under the Weave/Lead Agency program of the Swiss National Science Foundation and the National Science Centre of Poland through grant OPUS24+LAP No. 2022/47/I/NZ7/03112.

Competing interests. WMS and MC are full-time employees of Siemens Medical Solutions USA, Inc. HS is a part-time employee of Siemens Healthineers International AG. PM is an inventor on a patent related to this work. Patent nos.: (Poland) PL 227658, (Europe) EP 3039453, and (United States) US 9,851,456], filed (Poland) 30 August 2013, (Europe) 29 August 2014, and (United States) 29 August 2014; published (Poland) 23 January 2018, (Europe) 29 April 2020, and (United States) 26 December 2017. FC is currently supported by a research grant from Siemens Healthineers and receives speaker honoraria from Bracco AG and Pfizer AG for matters not related to the present manuscript. AR has received research support and speaker honoraria from Siemens. KS received research support from Novartis and Siemens and conference sponsorship from United Imaging, Siemens, and Subtle Medical not related to the submitted work. All other authors have no conflict of interests to report.

Ethics approval. This study was performed in line with the principles of the Declaration of Helsinki. The Kantonale Ethikkommission Bern approved the patient acquisitions (KEK-Nr. 2022–00486 and 2020-02903). All patients provided written informed consent for inclusion.

Data availability. Evaluated data from the ^{82}Rb dataset is available in the Zenodo repository https://doi.org/10.5281/zenodo.11243763. The remaining datasets generated and/or analysed during the current study are available from the corresponding author on reasonable request.

Consent to participate. Informed consent was obtained from all individual participants included in the study.

References

[1] Mohorovičić, S.: Möglichkeit neuer Elemente und ihre Bedeutung für die Astrophysik. Astronomische Nachrichten **253**(4), 93–108 (1934) https://doi.org/10.1002/asna.19342530402

[2] Deutsch, M.: Evidence for the formation of positronium in gases. Phys. Rev. **82**, 455–456 (1951) https://doi.org/10.1103/PhysRev.82.455

[3] Karshenboim, S.G.: Precision physics of simple atoms: QED tests, nuclear structure and fundamental constants. Phys. Rept. **422**, 1–63 (2005) https://doi.org/10.1016/j.physrep.2005.08.008 arXiv:hep-ph/0509010

[4] Moskal, P., Czerwiński, E., Raj, J., Bass, S.D., Beyene, E.Y., Chug, N., Coussat, A., Curceanu, C., Dadgar, M., Das, M., Dulski, K., Gajos, A., Gorgol, M., Hiesmayr, B.C., Jasińska, B., Kacprzak, K., Kaplanoglu, T., Kapłon, Ł., Klimaszewski, K., Konieczka, P., Korcyl, G., Kozik, T., Krzemień, W., Kumar, D., Moyo, S., Mryka, W., Niedźwiecki, S., Parzych, S., Río, E.P., Raczyński, L., Sharma, S., Choudhary, S., Shopa, R.Y., Silarski, M., Skurzok, M., Stępień, E.Ł., Tanty, P., Ardebili, F.T., Ardebili, K.T., Eliyan, K.V., Wiślicki, W.: Discrete symmetries tested at 10E4 precision using linear polarization of photons from positronium annihilations. Nature Communications **15**(1) (2024) https://doi.org/10.1038/s41467-023-44340-6

[5] Vértes, A., Nagy, S., Klencsár, Z., Lovas, R.G., Rösch, F.: Handbook of Nuclear Chemistry: Vol. 1: Basics of Nuclear Science. Handbook of Nuclear Chemistry. Springer New York, USA, ??? (2010). https://doi.org/10.1007/978-1-4419-0720-2

[6] Bass, S.D., Mariazzi, S., Moskal, P., Stępień, E.Ł.: Colloquium: Positronium physics and biomedical applications. Rev. Mod. Phys. **95**, 021002 (2023) https://doi.org/10.1103/RevModPhys.95.021002

[7] Hourlier, A., Boisson, F., Brasse, D.: Experimental Uses of Positronium and Potential for Biological Applications. IEEE Transactions on Radiation and Plasma Medical Sciences **8**(6), 581–594 (2024) https://doi.org/10.1109/TRPMS.2024.3407981

[8] Charlton, M., Humberston, J.W.: Positron Physics, 1st edn. Cambridge Monographs on Atomic, Molecular and Chemical Physics. Cambridge University Press, ??? (2001). http://www.cambridge.org/0521415500

[9] Gidley, D.W., Peng, H.-G., Vallery, R.S.: Positron annihilation as a method to characterize porous materials. Annual Review of Materials Research **36**(Volume 36, 2006), 49–79 (2006) https://doi.org/10.1146/annurev.matsci.36.111904.135144

[10] Stepanov, S.V., Byakov, V.M., Hirade, T.: To the theory of Ps formation. New interpretation of the e+ lifetime spectrum in water. Radiation Physics and Chemistry **76**(2), 90–95 (2007) https://doi.org/10.1016/j.radphyschem.2006.03.012 . Proceedings of the 8th International Workshop on Positron and Positronium Chemistry

[11] Stepanov, S.V., Byakov, V.M., Zvezhinskiy, D.S., Duplâtre, G., Nurmukhametov, R.R., Stepanov, P.S.: Positronium in a Liquid Phase: Formation, Bubble State and Chemical Reactions. Advances in Physical Chemistry **2012**(1), 431962 (2012) https://doi.org/10.1155/2012/431962

[12] Čížek, J.: Characterization of lattice defects in metallic materials by positron annihilation spectroscopy: A review. Journal of Materials Science & Technology **34**(4), 577–598 (2018) https://doi.org/10.1016/j.jmst.2017.11.050

[13] Takyu, S., Shibuya, K., Nishikido, F., Tashima, H., Takahashi, M., Yamaya, T.: Two-dimensional positronium lifetime imaging using certified reference materials. Applied Physics Express **15**(10), 106001 (2022) https://doi.org/10.35848/1882-0786/ac8d7b

[14] Champion, C., Loirec, C.L.: Positron follow-up in liquid water: II. Spatial and energetic study for the most important radioisotopes used in PET. Physics in Medicine & Biology **52**(22), 6605 (2007) https://doi.org/10.1088/0031-9155/52/22/004

[15] Axpe, E., Lopez-Euba, T., Castellanos-Rubio, A., Merida, D., Garcia, J.A., Plaza-Izurieta, L., Fernandez-Jimenez, N., Plazaola, F., Bilbao, J.R.: Detection of atomic scale changes in the free volume void size of three-dimensional colorectal cancer cell culture using positron annihilation lifetime spectroscopy. PloS one **9**, 83838 (2014) https://doi.org/10.1371/journal.pone.0083838

[16] Moskal, P., Jasińska, B., Stępień, E.Ł., Bass, S.D.: Positronium in medicine and biology. Nature Reviews Physics **1**(9), 527–529 (2019) https://doi.org/10.1038/s42254-019-0078-7

[17] Moskal, P., Kisielewska, D., Curceanu, C., Czerwiński, E., Dulski, K., Gajos, A., Gorgol, M., Hiesmayr, B., Jasińska, B., Kacprzak, K., Kapłon, Ł., Korcyl, G., Kowalski, P., Krzemień, W., Kozik, T., Kubicz, E., Mohammed, M., Niedźwiecki, S., Pałka, M., Pawlik-Niedźwiecka, M., Raczyński, L., Raj, J., Sharma, S., Shivani, Shopa, R.Y., Silarski, M., Skurzok, M., Stępień, E., Wiślicki, W., Zgardzińska, B.: Feasibility study of the positronium imaging with the J-PET tomograph. Physics in Medicine & Biology **64**, 055017 (2019) https://doi.org/10.1088/1361-6560/aafe20

[18] Moyo, S., Moskal, P., Stępień, E.: Feasibility study of positronium application for blood clots structural characteristics. Bio-Algorithms and Med-Systems **18**(1), 163–167 (2022) https://doi.org/10.2478/bioal-2022-0087

[19] Moskal, P., Kubicz, E., Grudzień, G., Czerwiński, E., Dulski, K., Leszczyński, B., Niedźwiecki, S., Ste pień, E.Ł.: Developing a novel positronium biomarker for cardiac myxoma imaging. EJNMMI Physics **10**, 22 (2023) https://doi.org/10.1186/s40658-023-00543-w

[20] Zaleski, R., Kotowicz, O., Górska, A., Zaleski, K., Zgardzińska, B.: Investigation of the ability to detect electrolyte disorder using PET with positron annihilation lifetime spectroscopy. The Journal of Physical Chemistry B **127**(46), 9887–9890 (2023) https://doi.org/10.1021/acs.jpcb.3c04208

[21] Karimi, H., Moskal, P., Żak, A., Stępień, E.Ł.: 3D melanoma spheroid model for the development of positronium biomarkers. Scientific Reports **13**(1), 7648 (2023) https://doi.org/10.1038/s41598-023-34571-4

[22] Avachat, A.V., Mahmoud, K.H., Leja, A.G., Xu, J.J., Anastasio, M.A., Sivaguru, M., Di Fulvio, A.: Ortho-positronium lifetime for soft-tissue classification. Scientific Reports **14**(1), 21155 (2024) https://doi.org/10.1038/s41598-024-71695-7

[23] Shibuya, K., Saito, H., Nishikido, F., Takahashi, M., Yamaya, T.: Oxygen sensing ability of positronium atom for tumor hypoxia imaging. Communications Physics (173) (2020) https://doi.org/10.1038/s42005-020-00440-z

[24] Stepanov, P.S., Selim, F.A., Stepanov, S.V., Bokov, A.V., Ilyukhina, O.V., Duplâtre, G., Byakov, V.M.: Interaction of positronium with dissolved oxygen in liquids. Physical chemistry chemical physics: PCCP **22**, 5123–5131 (2020) https://doi.org/10.1039/c9cp06105c

[25] Stepanov, S.V., Byakov, V.M., Stepanov, P.S.: Positronium in biosystems and medicine: A new approach to tumor diagnostics based on correlation between oxygenation of tissues and lifetime of the positronium atom. Physics of Wave Phenomena **29** (2021) https://doi.org/10.3103/S1541308X21020138

[26] Moskal, P., Stępień, E.Ł.: Positronium as a biomarker of hypoxia. Bio-Algorithms and Med-Systems **17**(4), 311–319 (2021) https://doi.org/10.1515/bams-2021-0189

[27] Takyu, S., Nishikido, F., Tashima, H., Akamatsu, G., Matsumoto, K.-i., Takahashi, M., Yamaya, T.: Positronium lifetime measurement using a clinical pet system for tumor hypoxia identification. Nuclear Instruments and Methods in Physics Research Section A: Accelerators, Spectrometers, Detectors and Associated Equipment **1065**, 169514 (2024) https://doi.org/10.1016/j.nima.2024.169514

[28] Takyu, S., Matsumoto, K.-i., Hirade, T., Nishikido, F., Akamatsu, G., Tashima, H., Takahashi, M., Yamaya, T.: Quantification of radicals in aqueous solution by positronium lifetime: an experiment using a clinical PET scanner. Japanese Journal of Applied Physics **63**(8), 086003 (2024) https://doi.org/10.

35848/1347-4065/ad679a

[29] Jasińska, B., Zgardzińska, B., Chołubek, G., Gorgol, M., Wiktor, K., Wysogld, K., Białas, P., Curceanu, C., Czerwiński, E., Dulski, K., et al.: Human tissues investigation using PALS technique. Acta Physica Polonica B **48**(10) (2017) https://doi.org/10.5506/APhysPolB.48.1737 arXiv:1711.04512

[30] Moskal, P., Baran, J., Bass, S., Choiński, J., Chug, N., Curceanu, C., Czerwiński, E., Dadgar, M., Das, M., Dulski, K., Eliyan, K.V., Fronczewska, K., Gajos, A., Kacprzak, K., Kajetanowicz, M., Kaplanoglu, T., Kapłon, Ł., Klimaszewski, K., Kobylecka, M., Korcyl, G., Kozik, T., Krzemień, W., Kubat, K., Kumar, D., Kunikowska, J., Ms czewska, J., Migdał, W., Moskal, G., Mryka, W., Niedźwiecki, S., Parzych, S., Rio, E.P., Raczyński, L., Sharma, S., Shivani, S., Shopa, R.Y., Silarski, M., Skurzok, M., Tayefi, F., Ardebili, K.T., Tanty, P., Wiślicki, W., Królicki, L., Stępień, E.Ł.: Positronium image of the human brain in vivo. Science Advances **10**(37), 2840 (2024) https://doi.org/10.1126/sciadv.adp2840

[31] Moskal, P.: Positronium Imaging. In: 2019 IEEE Nuclear Science Symposium and Medical Imaging Conference (NSS/MIC), pp. 1–3 (2019). https://doi.org/10.1109/NSS/MIC42101.2019.9059856

[32] Conti, M., Eriksson, L.: Physics of pure and non-pure positron emitters for PET: a review and a discussion. EJNMMI physics **3**, 8 (2016) https://doi.org/10.1186/s40658-016-0144-5

[33] Sitarz, M., Cussonneau, J.-P., Matulewicz, T., Haddad, F.: Radionuclide candidates for beta + gamma coincidence PET: An overview. Applied Radiation and Isotopes **155**, 108898 (2020) https://doi.org/10.1016/j.apradiso.2019.108898

[34] Korcyl, G., Białas, P., Curceanu, C., Czerwiński, E., Dulski, K., Flak, B., Gajos, A., Głowacz, B., Gorgol, M., Hiesmayr, B.C., Jasińska, B., Kacprzak, K., Kajetanowicz, M., Kisielewska, D., Kowalski, P., Kozik, T., Krawczyk, N., Krzemień, W., Kubicz, E., Mohammed, M., Niedźwiecki, S., Pawlik-Niedźwiecka, M., Pałka, M., Raczyński, L., Rajda, P., Rudy, Z., Salabura, P., Sharma, N.G., Sharma, S., Shopa, R.Y., Skurzok, M., Silarski, M., Strzempek, P., Wieczorek, A., Wiślicki, W., Zaleski, R., Zgardzińska, B., Zieliński, M., Moskal, P.: Evaluation of single-chip, real-time tomographic data processing on fpga soc devices. IEEE Transactions on Medical Imaging **37**(11), 2526–2535 (2018) https://doi.org/10.1109/TMI.2018.2837741

[35] Alberts, I., Hünermund, J.-N., Prenosil, G., Mingels, C., Bohn, K.P., Viscione, M., Sari, H., Vollnberg, B., Shi, K., Afshar-Oromieh, A., Rominger, A.: Clinical performance of long axial field of view PET/CT: a head-to-head intra-individual comparison of the Biograph Vision Quadra with the Biograph Vision PET/CT. European journal of nuclear medicine and molecular imaging **48**(8), 2395–2404 (2021)

[36] Slart, R.H.J.A., Rominger, A.: Collection on clinical total-body-PET studies. European journal of nuclear medicine and molecular imaging **50**, 1556–1557 (2023) https://doi.org/10.1007/s00259-023-06161-z

[37] Prenosil, G.A., Sari, H., Fürstner, M., Afshar-Oromieh, A., Shi, K., Rominger, A., Hentschel, M.: Performance characteristics of the Biograph Vision Quadra PET/CT system with a long axial field of view using the NEMA NU 2-2018 standard. Journal of nuclear medicine **63**, 476–484 (2022) https://doi.org/10.2967/jnumed.121.261972

[38] Spencer, B.A., Berg, E., Schmall, J.P., Omidvari, N., Leung, E.K., Abdelhafez, Y.G., Tang, S., Deng, Z., Dong, Y., Lv, Y., Bao, J., Liu, W., Li, H., Jones, T., Badawi, R.D., Cherry, S.R.: Performance evaluation of the uEXPLORER total-body PET/CT scanner based on NEMA NU 2-2018 with additional tests to characterize PET scanners with a long axial field of view. Journal of nuclear medicine **62**, 861–870 (2021) https://doi.org/10.2967/jnumed.120.250597

[39] Qi, J., Huang, B.: Positronium lifetime image reconstruction for TOF PET. IEEE transactions on medical imaging **41**, 2848–2855 (2022) https://doi.org/10.1109/TMI.2022.3174561

[40] Shibuya, K., Saito, H., Tashima, H., Yamaya, T.: Using inverse laplace transform in positronium lifetime imaging. Physics in Medicine & Biology **67**(2), 025009 (2022) https://doi.org/10.1088/1361-6560/ac499b

[41] Jegal, J., Jeong, D., Seo, E.-S., Park, H., Kim, H.: Convolutional neural network-based reconstruction for positronium annihilation localization. Scientific reports **12**, 8531 (2022) https://doi.org/10.1038/s41598-022-11972-5

[42] Shopa, R.Y., Dulski, K.: Positronium imaging in J-PET with an iterative activity reconstruction and a multi-stage fitting algorithm. Bio-Algorithms and Med-Systems **19**(1), 54–63 (2023)

[43] Huang, B., Li, T., Arino-Estrada, G., Dulski, K., Shopa, R.Y., Moskal, P., Stepien, E., Qi, J.: SPLIT: Statistical Positronium Lifetime Image Reconstruction via Time-Thresholding. IEEE transactions on medical imaging **43**, 2148–2158 (2024) https://doi.org/10.1109/TMI.2024.3357659

[44] Chen, Z., Kao, C.-M., Huang, H.-H., An, L.: Enhanced positronium lifetime imaging through two-component reconstruction in time-of-flight positron emission tomography. Frontiers in Physics **12** (2024) https://doi.org/10.3389/fphy.2024.1429344

[45] Steinberger, W.M., Sari, H., Mercolli, L., Parzych, S., Niedźwiecki, S., Lapkiewicz, G., Moskal, P., Stępień, E., Rominger, A., Shi, K., Conti, M.: Positronium lifetime measurements using 82rb in a long-axial fov pet/ct scanner. In: 2023 IEEE Nuclear Science Symposium, Medical Imaging Conference and

International Symposium on Room-Temperature Semiconductor Detectors (NSS MIC RTSD), pp. 1–2 (2023). https://doi.org/10.1109/NSSMICRTSD49126.2023.10338379

[46] Steinberger, W.M., Mercolli, L., Breuer, J., Sari, H., Parzych, S., Niedzwiecki, S., Lapkiewicz, G., Moskal, P., Stępień, E.Ł., Rominger, A., Shi, K., Conti, M.: Positronium lifetime validation measurements using a long-axial field-of-view positron emission tomography scanner. EJNMMI Physics **11**(76) (2024) https://doi.org/10.1186/s40658-024-00678-4

[47] McCutchan, E.A.: Nuclear Data Sheets for A=68. Nuclear Data Sheets **113**(6), 1735–1870 (2012) https://doi.org/10.1016/j.nds.2012.06.002

[48] Tuli, J.K., Browne, E.: Nuclear Data Sheets for A=82. Nuclear Data Sheets **157**, 260–494 (2019) https://doi.org/10.1016/j.nds.2019.04.002

[49] Katakura, J.-i., Wu, Z.D.: Nuclear Data Sheets for A=124. Nuclear Data Sheets **109**(7), 1655–1877 (2008) https://doi.org/10.1016/j.nds.2008.06.001

[50] Wasserthal, J., Breit, H.-C., Meyer, M.T., Pradella, M., Hinck, D., Sauter, A.W., Heye, T., Boll, D.T., Cyriac, J., Yang, S., Bach, M., Segeroth, M.: Totalsegmentator: Robust segmentation of 104 anatomic structures in ct images. Radiology: Artificial Intelligence **5**(5), 230024 (2023) https://doi.org/10.1148/ryai.230024

[51] Isensee, F., Jaeger, P.F., Kohl, S.A.A., Petersen, J., Maier-Hein, K.H.: nnU-Net: a self-configuring method for deep learning-based biomedical image segmentation. Nature methods **18**, 203–211 (2021) https://doi.org/10.1038/s41592-020-01008-z

[52] Mougeot, X.: Reliability of usual assumptions in the calculation of β and ν spectra. Physical Review C **91**, 055504 (2015) https://doi.org/10.1103/PhysRevC.91.055504

[53] White, R.D., Tattersall, W., Boyle, G., Robson, R.E., Dujko, S., Petrovic, Z.L., Bankovic, A., Brunger, M.J., Sullivan, J.P., Buckman, S.J., Garcia, G.: Low-energy electron and positron transport in gases and soft-condensed systems of biological relevance. Applied Radiation and Isotopes **83**, 77–85 (2014) https://doi.org/10.1016/j.apradiso.2013.01.008

[54] Kotera, K., Saito, T., Yamanaka, T.: Measurement of positron lifetime to probe the mixed molecular states of liquid water. Physics Letters A **345**(1), 184–190 (2005) https://doi.org/10.1016/j.physleta.2005.07.018

[55] Moskal, P., Dulski, K., Chug, N., Curceanu, C., Czerwiński, E., Dadgar, M., Gajewski, J., Gajos, A., Grudzień, G., Hiesmayr, B.C., Kacprzak, K., Kapłon, Ł., Karimi, H., Klimaszewski, K., Korcyl, G., Kowalski, P., Kozik, T., Krawczyk, N., Krzemień, W., Kubicz, E., Małczak, P., Niedźwiecki, S., Pawlik-Niedźwiecka,

M., Pędziwiatr, M., Raczyński, L., Raj, J., Ruciński, A., Sharma, S., Shivani, Shopa, R.Y., Silarski, M., Skurzok, M., Stępień, E.Ł., Szczepanek, M., Tayefi, F., Wiślicki, W.: Positronium imaging with the novel multiphoton PET scanner. Science advances **7**, 4394 (2021) https://doi.org/10.1126/sciadv.abh4394

[56] Gelman, A.: Prior distributions for variance parameters in hierarchical models. Bayesian Analysis **1**(3), 515–534 (2006) https://doi.org/10.1214/06-BA117A

[57] Hoffman, M.D., Gelman, A.: The No-U-Turn sampler: adaptively setting path lengths in Hamiltonian Monte Carlo. Journal of Machine Learning Research **15**(1), 1593–1623 (2014) https://doi.org/10.48550/arXiv.1111.4246 arXiv:1111.4246 [stat.CO]

[58] Bezanson, J., Edelman, A., Karpinski, S., Shah, V.B.: Julia: A fresh approach to numerical computing. SIAM review **59**(1), 65–98 (2017)

[59] Ge, H., Xu, K., Ghahramani, Z.: Turing: a language for flexible probabilistic inference. In: International Conference on Artificial Intelligence and Statistics, AISTATS 2018, 9-11 April 2018, Playa Blanca, Lanzarote, Canary Islands, Spain, pp. 1682–1690 (2018). http://proceedings.mlr.press/v84/ge18b.html

[60] Kumar, R., Carroll, C., Hartikainen, A., Martin, O.: ArviZ a unified library for exploratory analysis of bayesian models in python. Journal of Open Source Software **4**(33), 1143 (2019) https://doi.org/10.21105/joss.01143

[61] Gelman, A., Carlin, J.B., Stern, H.S., Dunson, D.B., Vehtari, A., Rubin, D.B.: Bayesian Data Analysis, 3rd ed. edn. Chapman & Hall/CRC texts in statistical science series. CRC Press, ??? (2014). http://www.stat.columbia.edu/ gelman/-book/

[62] Vehtari, A., Simpson, D., Gelman, A., Yao, Y., Gabry, J.: Pareto Smoothed Importance Sampling. Journal of Machine Learning Research (25), 1–58 (2024) https://doi.org/10.48550/arXiv.1507.02646 arXiv:1507.02646 [stat.CO]

[63] Vehtari, A., Gelman, A., Gabry, J.: Practical Bayesian model evaluation using leave-one-out cross-validation and WAIC. Statistics and Computing **27**(5), 1413–1432 (2017) https://doi.org/10.1007/s11222-016-9696-4

[64] Sivula, T., Magnusson, M., Matamoros, A.A., Vehtari, A.: Uncertainty in Bayesian Leave-One-Out Cross-Validation Based Model Comparison (2023). https://doi.org/10.48550/arXiv.2008.10296 . https://arxiv.org/abs/2008.10296

[65] Parada, C.: ParetoSmooth.jl (2021). https://github.com/TuringLang/ParetoSmooth.jl

[66] Parzych, S., Baran, J., Beyene, E.Y., Conti, M., Coussat, A., Chug, N., Curceanu, C., Czerwiński, E., Dadgar, M., Dulski, K., Eliyan, K.V., Gajos, A., Hiesmayr,

B., Jędruszczak, A., Kacprzak, K., Kajetanowicz, M., Kaplanoglu, T., Kapłon, L., Klimaszewski, K., Korcyl, G., Kozik, T., Krzemień, W., Kumar, D., Lapkiewicz, G., Mercolli, L., Migdał, W., Moyo, S., Mryka, W., Niedźwiecki, S., Del Río, E.P., Raczyński, L., Rominger, A., Sari, H., Sharma, S., Shi, K., Shivani, S., Shopa, R., Skurzok, M., Steinberger, W.M., Stępień, E., Tanty, P., Tayefi, F., Ardebili, K.T., Wiślicki, W., Moskal, P.: Feasibility study of positronium imaging with Biograph Vision Quadra and Modular J-PET. In: 2023 IEEE Nuclear Science Symposium, Medical Imaging Conference and International Symposium on Room-Temperature Semiconductor Detectors (NSS MIC RTSD), pp. 1–2 (2023). https://doi.org/10.1109/NSSMICRTSD49126.2023.10338478

[67] Ma, B., Wen, S., Luo, Y., Zhang, T., Yang, Y., Shen, C., Zhang, Y., Ji, Q., Qu, N., Wang, Y.: Targeting Tumor Hypoxia Inhibits Aggressive Phenotype of Dedifferentiated Thyroid Cancer. The Journal of Clinical Endocrinology & Metabolism **108**(2), 368–384 (2022) https://doi.org/10.1210/clinem/dgac548

[68] Horn, J.D., Wu, F., Corsiglia, G., Jean, Y.C.: Asymmetric positron interactions with chiral quartz crystals? In: Positron Annihilation - ICPA-17. Defect and Diffusion Forum, vol. 373, pp. 221–226. Trans Tech Publications Ltd, ??? (2017). https://doi.org/10.4028/www.scientific.net/DDF.373.221

[69] Stepanov, S.V., Zvezhinskiy, D., Duplâtre, G., Byakov, V., Batskikh, Y.Y., Stepanov, P.S.: Incorporation of the magnetic quenching effect into the blob model of Ps formation. finite sized Ps in a potential well. In: Materials Science Forum, vol. 666, pp. 109–114 (2011). https://doi.org/10.4028/www.scientific.net/MSF.666.109

[70] Byrne, A.L., Bennett, M., Chatterji, R., Symons, R., Pace, N.L., Thomas, P.S.: Peripheral venous and arterial blood gas analysis in adults: are they comparable? a systematic review and meta-analysis. Respirology **19**(2), 168–175 (2014) https://doi.org/10.1111/resp.12225

[71] Arbiol-Roca, A., Imperiali, C.E., Dot-Bach, D., Valero-Politi, J., Dastis-Arias, M.: Stability of pH, blood gas partial pressure, hemoglobin oxygen saturation fraction, and lactate concentration. Annals of laboratory medicine **40**(6), 448–456 (2020) https://doi.org/10.3343/alm.2020.40.6.448